JACS
JOURNAL OF THE AMERICAN CHEMICAL SOCIETY
Article
pubs.acs.org/JACS

Ionization of High-Density Deep Donor Defect States Explains the Low Photovoltage of Iron Pyrite Single Crystals

Miguel Cabán-Acevedo, Nicholas S. Kaiser, Caroline R. English, Dong Liang, Blaise J. Thompson, Hong-En Chen, Kyle J. Czech, John C. Wright, Robert J. Hamers, and Song Jin*

Department of Chemistry, University of Wisconsin—Madison, 1101 University Avenue, Madison, Wisconsin 53706, United States

Supporting Information

ABSTRACT: Iron pyrite (FeS_2) is considered a promising earth-abundant semiconductor for solar energy conversion with the potential to achieve terawatt-scale deployment. However, despite extensive efforts and progress, the solar conversion efficiency of iron pyrite remains below 3%, primarily due to a low open circuit voltage (V_{OC}). Here we report a comprehensive investigation on {100}-faceted *n*-type iron pyrite single crystals to understand its puzzling low V_{OC}. We utilized electrical transport, optical spectroscopy, surface photovoltage, photoelectrochemical measurements in aqueous and acetonitrile electrolytes, UV and X-ray photoelectron spectroscopy, and Kelvin force microscopy to characterize the bulk and surface defect states and their influence on the semiconducting properties and solar conversion efficiency of iron pyrite single crystals. These insights were used to develop a circuit model analysis for the electrochemical impedance spectroscopy that allowed a complete characterization of the bulk and surface defect states and the construction of a detailed energy band diagram for iron pyrite crystals. A holistic evaluation revealed that the high-density of intrinsic surface states cannot satisfactorily explain the low photovoltage; instead, the ionization of high-density bulk deep donor states, likely resulting from bulk sulfur vacancies, creates a nonconstant charge distribution and a very narrow surface space charge region that limits the total barrier height, thus satisfactorily explaining the limited photovoltage and poor photoconversion efficiency of iron pyrite single crystals. These findings lead to suggestions to improve single crystal pyrite and nanocrystalline or polycrystalline pyrite films for successful solar applications.

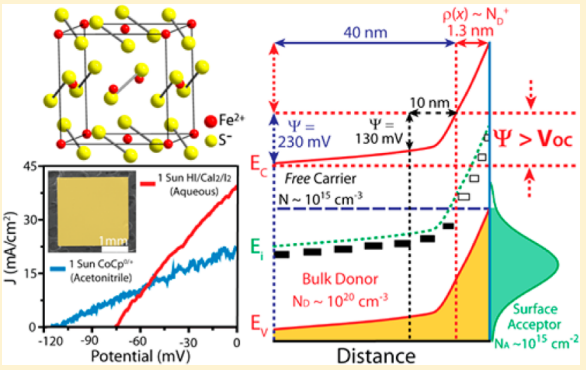

INTRODUCTION

Iron pyrite (cubic FeS_2) is a semiconducting first-row transition metal dichalcogenide that holds promise as a cost-effective solar material due to its earth-abundance, suitable band gap (in the range of E_g = 0.80−0.95 eV), and large absorption coefficient ($\alpha \sim 6 \times 10^5$ cm^{-1} for $h\nu$ > 1.3 eV).[1,2] Bulk *n*-type iron pyrite single crystals can have high majority carrier mobilities (up to 360 cm^2 V^{-1} s^{-1}) and long minority carrier diffusion lengths (L = 0.1−1 μm).[1,3−5] Thus, iron pyrite has the theoretical potential for developing sustainable and inexpensive solar cell technologies at the terawatt scale.[6] These promising properties have motivated research efforts that have aggressively targeted the synthesis of iron pyrite materials using a wide variety of methods, including chemical vapor transport (CVT),[7−9] chemical vapor deposition,[10,11] thermal sulfidation of various precursor materials,[12−15] and promising cost-effective alternatives such as the colloidal synthesis of nanocrystals.[16−22] Despite extensive efforts and significant progress in synthesis, the solar energy conversion efficiency for iron pyrite solar devices has remained below 2.8% since the beginning of the 1990s.[23] This often claimed efficiency was reported for a photoelectrochemical (PEC) solar cell using a CVT grown, extrinsically doped *n*-type pyrite single crystal and an iodine/iodide aqueous electrolyte with little experimental detail.[23] The photoanode reached an outstanding photocurrent of 42 mA/cm^2 at short circuit, but its efficiency was ultimately limited by a low open circuit voltage ($V_{OC} \leq$ 187 mV) and moderate fill factor (~50%).[23] Additionally, this report of a modest V_{OC} is one of only three known examples for any iron pyrite material,[2,23,24] all of which were done in the late 1980s and early 1990s by the Tributsch group and collaborators.[1,23] (Note that none of the recent reports of iron pyrite nanocrystals, or nanocrystalline or polycrystalline films of iron pyrite has demonstrated photovoltage.) However, a lack of important synthetic details and explicit discussion of the factors controlling the performance of these solar devices has limited the understanding of iron pyrite. Clearly, understanding the reason for the low performance is essential for improving iron pyrite as a solar material; and such understanding can also be generally useful for evaluating and improving other next-generation solar materials.[25−27]

Since the late 1980s, the existence of intrinsic surface states with a negative impact to Fermi level pinning and surface

Received: September 4, 2014
Published: November 15, 2014

   dx.doi.org/10.1021/ja509142w | J. Am. Chem. Soc. 2014, 136, 17163−17179

recombination mechanisms has been used as the main explanation for the low V_{OC} of iron pyrite single crystals.[23,28] However, a pinning of the surface Fermi level at an energy that could limit the barrier height in the space charge region has not been confirmed or supported by valence band studies performed for vacuum cleaved {100}-faceted iron pyrite single crystals. Instead the surface Fermi level has been observed near the valence band maximum,[29,30] which should result in a large barrier height. On the other hand, it was recently hypothesized using scanning tunneling spectroscopy (STS) and density function theory,[31] that the presence of surface states on a cleaved {100} surface can lead to narrowing of the surface band gap which could have implications for surface recombination. Nevertheless, it is important to note that the 3% solar conversion efficiency has been achieved after treatments of iron pyrite single crystals through electrochemical cathodic polarization in sulfuric acid.[5,32−34] Thus, is not clear whether the efficiency of such electrochemically treated iron pyrite materials has been limited by the surface defects hypothesized for a cleaved {100} surface with dangling bonds.[35]

An alternative hypothesis for the low V_{OC} of iron pyrite is detrimental bulk defect states. In particular, given the potential low energy of formation for intrinsic sulfur vacancies,[36] the existence of intrinsic bulk midgap donor states was predicted from ligand field theory (LFT) modeling of bulk sulfur vacancies.[37] Despite an absence of experimental evidence in this study, Bronold et al.[37] intuitively inferred that the space charge region or band bending near the surface could be modified due to the presence of bulk midgap states, leading to the formation of a surface tunneling region (called "triangular layer") that could explain the low V_{OC} of iron pyrite. In contrast, it was recently suggested that the formation of a surface inversion layer is responsible for the tunneling region inferred by Bronold et al.[37] and the low V_{OC} of iron pyrite.[38] From a classical band bending perspective, the formation of a surface inversion region can occur on any semiconductor when the surface Fermi level reaches an energy at which the charge density is dominated by the population of minority carriers (about twice the energy separation between the bulk and intrinsic Fermi level, $2\Psi_B$, for the classical case). As has been experimentally reported for PEC cells, aligning the surface Fermi level closer to the valence band edge should result in a large barrier height and large V_{OC}.[39−41] Therefore, the formation of a surface inversion region is an unsatisfactory explanation for the low solar conversion efficiency of iron pyrite single crystals.

Currently, there is still no consensus to whether the low photovoltage and solar conversion efficiency of iron pyrite single crystals is caused by surface or bulk states. Recent efforts to understand the intrinsic properties of iron pyrite have inadvertently neglected the intrinsic bulk states as an important hypothesis and primarily focused on the study of the surface electronic structure. This may have been caused by the hiatus in the studies of bulk iron pyrite single crystals since the mid-1990s and the resurgent interest in pyrite with the recent synthetic progress in pyrite nanomaterials.[12,14,16−20,42] However, it is important to make clear distinctions when discussing the limitations of nanocrystalline and polycrystalline thin films, and *n*-type pyrite single crystals, since they exhibit significantly different properties. Nanocrystalline and polycrystalline pyrite thin films have consistently been reported to exhibit an apparent heavily p-like conductivity[43] and a lack of photovoltage,[15,16,44] regardless of the synthetic methods. These experimental observations suggest that intrinsic defects may impose different limitations to the properties and performance of nanocrystalline and polycrystalline thin films in comparison to bulk *n*-type single crystals of pyrite. Such differences could be a result from the added complexity of grain boundary interactions among crystalline domains in a thin film. Hence, iron pyrite single crystals still provide the most well-defined platform to characterize and understand the *intrinsic* defects, which can then serve as a foundation to evaluate their impacts on different iron pyrite materials.

To understand and address the limitations imposed by defect states on the space charge properties of iron pyrite, we conducted a comprehensive investigation on the semiconducting, electrochemical, and interfacial properties of {100}-faceted *n*-type iron pyrite single crystals grown via CVT using high purity precursors. This manuscript is organized as the following: We first investigated the bulk semiconducting properties using electrical transport, UV−vis-NIR, surface photovoltage, and ultrafast reflective pump−probe measurements. Then the photoelectrochemical performance of the pyrite single crystals was studied using a wide variety of redox couples in both aqueous and acetonitrile (nonaqueous, aprotic) solvents. The energetic position of the surface Fermi level after chemical etching and electrochemical cleaning of the pyrite single crystals was then studied through UV and X-ray photoelectron spectroscopy and Kelvin force microscopy. Furthermore, we studied the surface sulfur chemical species of iron pyrite through angle-resolved X-ray photoelectron spectroscopy. Using the insights gleaned from these studies we developed an analogous circuit model analysis for the electrochemical impedance spectroscopy of *n*-type iron pyrite single crystals, which enabled the characterization of the energetic positions and densities of bulk and surface defects, and the construction of a detailed energy band diagram. Finally, a holistic evaluation revealed the fundamental limitations imposed by bulk defects on the solar efficiency of iron pyrite and their implications will be discussed.

RESULTS

Single Crystal Growth and Structural Characterization. Cubes of iron pyrite single crystals with {100} facets (Figure 1a) were grown by means of chemical vapor transport (CVT) using iron(II) chloride ($FeCl_2$) as the transporting agent and synthetic iron pyrite powder as the precursor material. The synthesis was carried out in a sealed ampule by heating high purity iron (99.998%) and sulfur (99.999%) powder at 600 °C. Subsequently, the CVT reaction was carried out in a different ampule using a temperature gradient of 650−550 °C for the precursor and deposition zone, respectively (see Supporting Information for details). The deposition product at the cold end of the ampule (Figure 1a) consisted mainly of square-faceted iron pyrite single crystals with dimensions ranging from hundreds of micrometers to as large as a few millimeters. The growth rate with $FeCl_2$ transporting agent was found to be ≈20 mg/h. While faster growth rates (≈ 40 mg/h) could be achieved when using iron(II) bromide as the transporting agent, the main products consisted of multifaceted crystals. In all of our subsequent studies, we analyzed only square-faceted iron pyrite single crystals grown with $FeCl_2$ as the transporting agent and we will refer to them as pyrite single crystals.

The phase identity of the as-synthesized single crystals and synthetic precursor powder was confirmed using powder X-ray diffraction (PXRD) (Figure 1b). All peaks in the PXRD

dx.doi.org/10.1021/ja509142w | J. Am. Chem. Soc. 2014, 136, 17163−17179

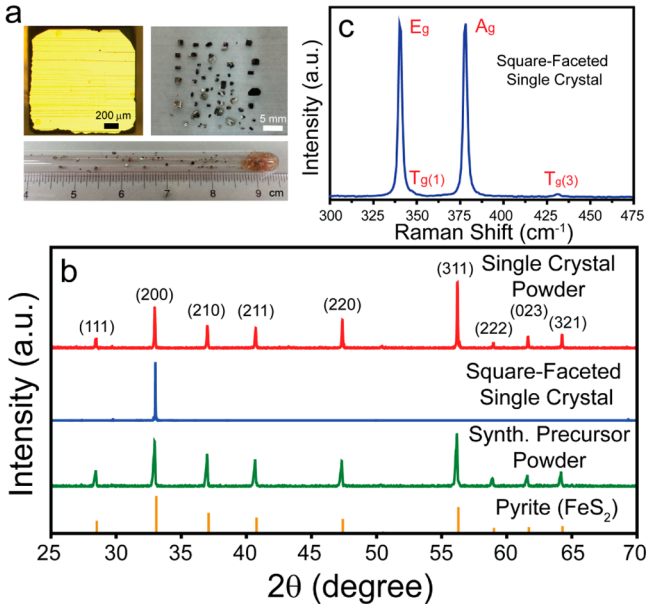

Figure 1. Structural characterization of the iron pyrite single crystals synthesized via CVT using the $FeCl_2$ transporting agent. (a) Optical images of the single crystal products and the quartz ampule CVT reactor. (b) PXRD taken for a powder sample prepared from crushed single crystals, a square-faceted single crystal, and the synthetic iron pyrite precursor powder, in comparison with the reference diffraction pattern for iron pyrite (JCPDS #65-3321). (c) Confocal micro-Raman spectroscopy of a square-faceted pyrite single crystal using a 532 nm excitation laser.

diffractogram for a powder sample prepared from crushed single crystals can be indexed exclusively to iron pyrite (cubic FeS_2, JCPDS #65-3321; space group $Pa\bar{3}$, a = 5.419 Å). In contrast, the PXRD pattern of an individual square-faceted single crystal shows only (200) diffraction, indicating that the crystal orientation is along [100], as expected for a square crystal habitat. Furthermore, we used confocal micro-Raman spectroscopy to confirm the phase purity of the pyrite single crystals (Figure 1c). The Raman spectrum shows three peaks corresponding to the characteristic active modes for bulk iron pyrite of S_2 libration (E_g), S–S in-phase stretch (A_g), and coupled libration and stretch (triply degenerated, specifically $T_{g(3)}$) modes.[45,46] The marcasite polymorph was never detected by PXRD or Raman, as expected for our synthetic temperature range, since marcasite is a kinetically stable phase.[47]

Electrical Transport Properties. We investigated the electrical transport properties, majority carrier type, and *free* carrier concentration of the as-grown pyrite single crystals through measurements of the temperature dependence of the electrical resistivity and Hall effect (see Supporting Information for details). The resistivity-temperature dependence data was best fitted with two different conduction regimes (Figure 2a,b). Conduction in the high temperature regime is dominated by the thermal activation of majority carriers (Figure 2a):[48]

$$\rho = \rho_0 \exp(E_a/k_B T) \quad (1)$$

According to the negative Hall coefficient (Figure 2c), the high temperature conduction regime corresponds to the thermal activation of electrons with an activation energy (E_a) of 226 ± 6 meV. Using E_a, we calculated the energetic position of the donor state (E_D) to be 452 ± 12 meV below the conduction band edge. Using $R_H = 1/(N \cdot e)$, the bulk *free* electron concentration (N) was calculated from the Hall coefficient at room temperature to be $N = 1.1 \times 10^{15}$ cm^{-3}. The low *free* carrier concentration and large thermal activation energy are indicative of a large density of deep donor states in the *n*-type pyrite single crystals. We calculated the density of donor states (N_D) using the classical assumption that the ionization of donor states (N_D^+) follows a Fermi–Dirac distribution:[48]

$$N_D^+(E_F) = \frac{N_D}{1 + g_D \exp((E_F - E_D)/k_B T)} \quad (2)$$

where g_D is the degeneracy of the donor states, and E_F is the bulk Fermi level, calculated using the effective density of states at the conduction band edge of $N_C = 3 \times 10^{18}$ cm^{-3} and *free* carrier concentration.[3] We hypothesize that the deep donor states result from intrinsic sulfur vacancies considering that our iron pyrite single crystals were synthesized using high purity precursors (no less than 99.998%) and taking into account previous reports on the intrinsic stoichiometry of high temperature pyrite.[36,49] Ligand field theory calculations by Bronold et al.[37] predicted the possibility of a doubly degenerated deep donor state resulting from S^{2-} species accompanying the intrinsic sulfur vacancies. Therefore, we used $g_D = 4$ as a first approximation. Then, using eq 2, E_D, and N at room temperature, the density of donor states was estimated to be $N_D = (7.6 \pm 3.3) \times 10^{19}$ cm^{-3} according to the high temperature transport properties. In the case of a singly or triply degenerated deep donor state, the density would be $N_D = (1.14 \pm 0.49) \times 10^{20}$ cm^{-3} and $N_D = (3.8 \pm 1.6) \times 10^{19}$ cm^{-3}, respectively.

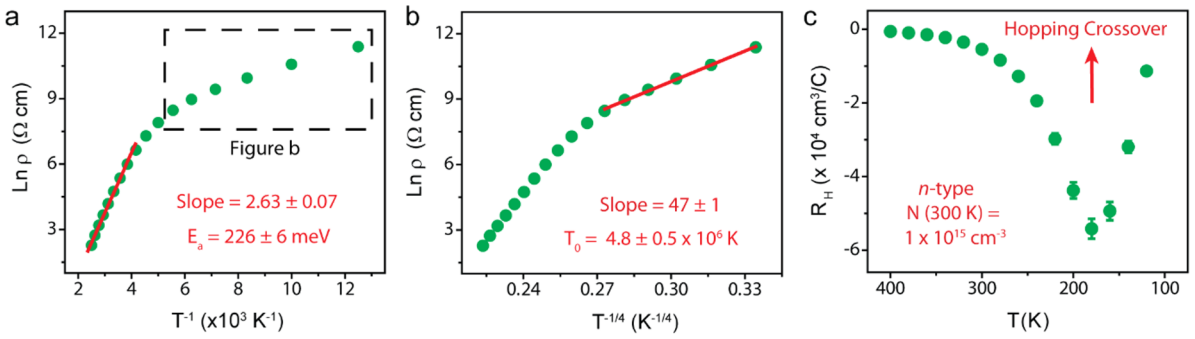

Figure 2. Electrical transport properties of a representative {100}-faceted iron pyrite single crystal. (a) High temperature resistivity plotted as Ln(ρ) vs $1/T$ and (b) low temperature resistivity plotted as Ln(ρ) vs $T^{-1/4}$. A current of 5 μA was applied. (c) Hall coefficients as a function of temperature for a representative Hall device of a millimeter sized single crystal with device dimensions of 0.560 mm (l) × 1.118 mm (w) × 1.284 mm (h).

dx.doi.org/10.1021/ja509142w | J. Am. Chem. Soc. 2014, 136, 17163–17179

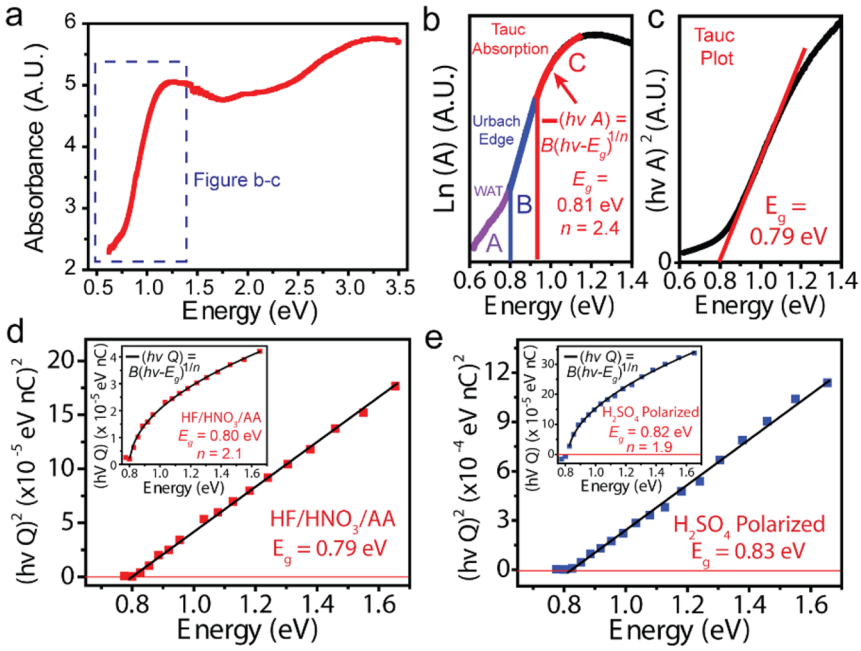

Figure 3. Optical and optoelectronic properties of iron pyrite. (a) UV−vis-NIR spectra for the internal absorbance, (b) the corresponding Ln(A) vs energy plot and (c) the corresponding Tauc plot for an iron pyrite powder sample prepared from crushed single crystals. (d and e) Tauc plots constructed from surface photovoltage (SPV) measurements on {100}-faceted iron pyrite single crystals. The SPV signal was converted to a photoinjected charge (Q_{ph}) in order to perform the analysis. The figure insets show the fitting of the measured Q_{ph} to a band-to-band optical transition equation, demonstrating that Q_{ph} is proportional to the absorption coefficient. The single crystal was precleaned prior to the TR-SPV measurements (inset) using (d) $HF/HNO_3/AA$ (1:2:1) and (e) cathodic polarization in 0.5 M H_2SO_4, sourcing −15 mA/cm^2 for 3−5 min.

In the low temperature regime, carrier transport proceeds through hopping following the variable range hopping (VRH) dependence (Figure 3b):[50]

$$\rho = \rho_0 \exp(T_0/T)^{1/4} \tag{3}$$

where T_0 is the characteristic temperature and ρ_0 is a constant or weakly temperature dependent prefactor. From linear fitting of $\ln(\rho)$ vs $1/T^{1/4}$ (Figure 2b), we determined that $T_0 = 4.8 \times 10^6$ K. In crystalline n-type semiconductors, VRH is a conduction mechanism that describes the hopping of carriers among localized states with similar energy but variable distance within a donor band.[50−53] VRH has been previously reported as a low temperature conduction mechanism in iron pyrite single crystals and polycrystalline films.[42,54,55] In the case of pyrite single crystals, the observation of VRH conduction at low temperature is consistent with the high density of deep donor states revealed by high temperature transport measurements. The precise temperature crossover is dependent on the density and distribution of donor states, in other words the donor bandwidth.[50,52,53]

In the low temperature Hall effect, we observed an increase in the Hall coefficient (R_H) which coincides with the transition to VRH conduction (Figure 2c). This minimum in the Hall coefficient can be explained using a two band model, where conduction in pyrite single crystals proceeds either by conduction band (σ_c, R_c) or hopping (σ_h, R_h). Therefore, the Hall coefficient can be expressed as[53,56]

$$R_H = \frac{\sigma_c^2 R_c + \sigma_h^2 R_h}{(\sigma_c + \sigma_h)^2} \tag{4}$$

where σ and R are the corresponding conductivities and Hall coefficients. At high temperatures, the conduction mechanism is dominated by the thermal activation of carriers into the conduction band. Therefore, $\sigma_c \gg \sigma_h$ and the Hall coefficient has the classical solution $R_H = R_c = 1/(e{\cdot}N) \approx T^{3/2} \exp(E_a/k_BT)$. On the other hand, at sufficiently low temperature, hopping conduction becomes the dominant conduction mechanism. Consequently, $\sigma_c \ll \sigma_h$ and the Hall coefficient will transition toward the hopping Hall coefficient (R_h). In the hopping regime, the absolute value of the Hall coefficient (R_H) is small or is assumed to be negligible;[51,57] thus the transition region for an n-type semiconductor is characterized by a minimum in the Hall coefficient.[56,58,59] Therefore, the temperature dependent Hall effect provides supporting evidence for low temperature hopping conduction. Additionally, there is a small change of only a factor of 4 in the Hall coefficient or *free* carrier concentration between room temperature to the hopping crossover temperature. This small change in *free* carrier concentration suggests the presence of localized deep donor states near the bulk Fermi level which is consistent with a high density of deep donor states and a wide deep donor band.

Optical and Optoelectronic Properties. We characterized the band gap energy (E_g) of the pyrite single crystals using integrating sphere UV−vis-NIR and surface photovoltage (SPV) measurements. From the internal absorbance (Figure 3a), we observed two strong absorption onsets at ∼0.80 and ∼2.0 eV, in addition to sub-band gap absorption. The first absorption onset can be divided into three types of optical transitions related to excitation between localized/tail states, tail states and extended states, and extended states; which are characteristic of semiconductors with a high density of defect states.[60,61] These optical transitions are labeled as region A, B, and C, respectively, in a plot of Ln(A) vs E (Figure 3b). The optical transitions A and B are known as weak absorption tail (WAT) and Urbach edge and can operate at energies below the fundamental band gap. In the Urbach edge the absorption

dx.doi.org/10.1021/ja509142w | J. Am. Chem. Soc. 2014, 136, 17163−17179

follows a characteristic exponential relationship with energy (called Urbach rule),[60,61] as observed for region B in Figure 3b. In Region C, the excitation occurs between the valence band and conduction band (extended states), thus it follows a band-to-band optical absorption equation: $(h\nu A) = \mathbf{B}(h\nu - E_g)^{1/n}$, where **B** is the matrix element and assumed to be constant. Through fitting using the band-to-band optical absorption equation (Figure 3b, red curve in region C) the type of optical transition was objectively determined to be direct ($n \sim 2$) and a band gap of E_g = 0.81 eV was obtained. The band gap energy can also be determined though linear extrapolation using a Tauc plot ($(h\nu A)^n$ vs E), from which E_g = 0.79 eV was obtained for n = 2 (Figure 3c). The optical band gap falls within the range of recently reported experimental values of 0.80−1.0 eV for iron pyrite,[1,14,19,62] but the optically direct transition appears inconsistent with the indirect band gap of iron pyrite. However, in the presence of a high density of defect states, the optical transition for an indirect semiconductor can become direct (n = 2) since momentum conservation can be achieved through mechanisms such as impurity scattering.[60]

We measured the SPV as a function of energy on a representative pyrite single crystal using a capacitor-like arrangement (see Supporting Information and Figure S1 for complete details).[63] The photovoltage was converted to a photocurrent and the photoinjected charge (Q_{ph}) was determined by integration. The sign of the photoinjected charge corresponds to the accumulation of holes (minority carriers) at the surface in our experimental setup, indicating an upward band bending in the space charge region. The SPV signal was experimentally shown to be proportional to the absorption coefficient by fitting the photoinjected charge to a band-to-band optical transition equation, and then a Tauc plot was constructed based on the obtained optical transition (n). Figure 3d shows the fitting to a band-to-band optical transition equation (inset) and corresponding Tauc plot (main figure) for a pyrite single crystal after pretreatment for 30 s in an isotropic etching solution consisting of hydrofluoric acid, nitric acid and acetic acid (HNA etching) in a 1:2:1 volume ratio.[28] We obtained an optically direct transition (i.e., n = 2) from the fitting and a band gap of 0.79 eV from the corresponding Tauc plot, which is in agreement with the optical band gap obtained from UV−vis-NIR measurements. We also measured the TR-SPV for the same single crystal after cathodic polarization in 0.5 M sulfuric acid (H_2SO_4) using a current of −15 mA/cm^2 for 3−5 min. This pretreatment has been employed and proposed to partially passivate bulk defects in iron pyrite,[5,32,33] and we will refer to this as electrochemical cleaning. In comparison to HNA etching, after electrochemical cleaning, we observed that the direct band gap increases to 0.83 eV (Figure 3e), which suggests that the optical properties of pyrite single crystals are heavily affected by defects in the materials. Indeed, it has been hypothesized that the variations in the band gap energy and optical transition of synthetic iron pyrite can be caused by sulfur vacancies either due to the formation of near conduction band defects[36,37] or direct conduction band lowering due to changes in unit cell parameters with sulfur stoichiometry.[49,64] Therefore, the observed optical properties for pyrite single crystals are consistent with the presence of a high density of bulk states and sulfur vacancies.

We also determined the carrier lifetime dynamics of the pyrite single crystals through ultrafast pump−probe spectroscopy measurements in a reflective geometry using a 800 nm pump and an 1190 nm probe, each with a 50 fs FWHM (see Supporting Information for details). The transient reflectivity spectra show an increase in the pyrite single crystal reflectivity for a short time after pumping, followed by a well time-separated exponential decay with a time constant (τ) of 288 ± 22 ps (Figure 4, black trace). We observed no statistical

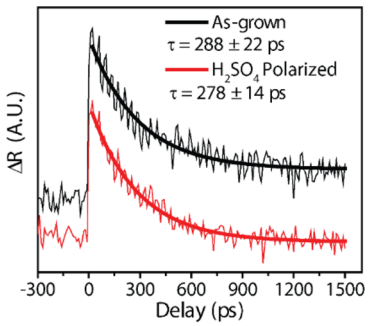

Figure 4. Carrier lifetime dynamics of the {100}-faceted iron pyrite single crystals measured with ultrafast reflective pump−probe spectroscopy using a 800 nm pump and an 1190 nm probe, each with a 50 fs FWHM and a 300 μm beam diameter. Curves were offset for clarity.

differences in the carrier lifetime of electrochemically cleaned pyrite single crystals (Figure 4, red trace). Both measurements on synthetic pyrite were similar to polished natural pyrite samples (see Figure S2 in the Supporting Information). This observed time constant for pyrite single crystals can be considered as an upper limit for the carrier lifetime within the absorption volume, since no longer lifetime dynamics were observed through pump−probe spectroscopy measurements or through TR-SPV measurements using a 3 ns pulse laser (see Figure S1b in the Supporting Information).

Photoelectrochemical Properties of Single Crystal Pyrite Liquid Junction Solar Cells. The photoelectrochemical (PEC) response of the pyrite single crystals was studied in a liquid junction solar cell configuration using platinum mesh as the counter electrode, in a variety of aqueous and nonaqueous electrolytes (see Supporting Information for details). Prior to measurements, all pyrite electrodes were electrochemically cleaned in 0.5 M H_2SO_4, by sourcing −15 mA/cm^2 for 3−5 min. Mechanical polishing of the electrode surfaces was avoided at all times, since we observed that polishing resulted in electrodes with a metal-like PEC response that could only be recovered after electrochemical cleaning (see Figure S3 in the Supporting Information). It has been previously hypothesized that mechanical polishing damages a sample volume that extends from the surface to ∼1 μm deep into the bulk of pyrite.[5,33] Figure 5a shows the PEC response for our champion electrode, with which a solar energy conversion efficiency of up to 0.83% was obtained in aqueous electrolyte under 1 sun illumination. The largest J_{SC} was 40 mA/cm^2 when using the aqueous electrolyte 4 M HI/1 M CaI_2/0.5 M I_2, but as seen from the J−V characteristics, the performance was limited by a low V_{OC} of 75 mV and a low fill factor of 28%. When cobaltocene/cobaltocenium ($CoCp_2^{0/+}$) redox couple in acetonitrile (a nonaqueous aprotic solvent) was used, the V_{OC} was improved to 115 mV but the J_{SC} was lower. The lower J_{SC} for the acetonitrile-based electrolyte could be inherent to the lower concentration of $CoCp_2$ redox couples, in comparison to the highly concentrated I_2/I^- redox couples in aqueous electrolyte. Furthermore, it has been previous suggested that the I^-/I_2 redox couple could facilitate electron transfer through

dx.doi.org/10.1021/ja509142w | J. Am. Chem. Soc. 2014, 136, 17163−17179

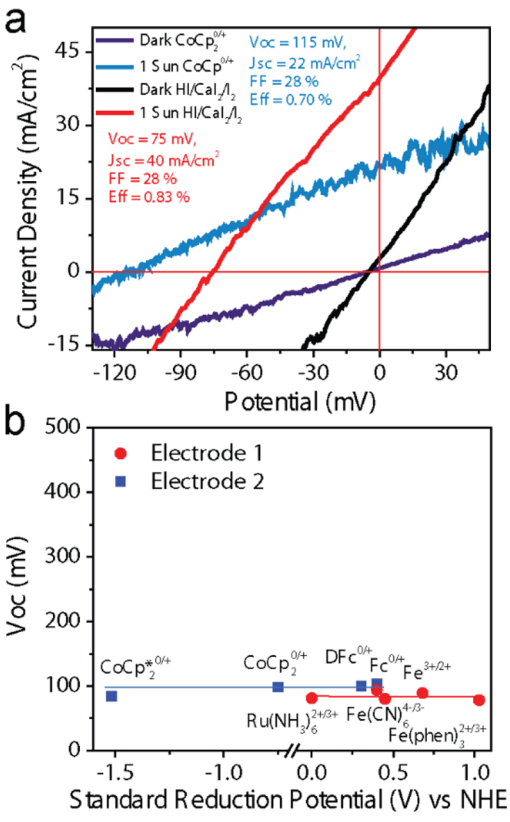

Figure 5. Photoelectrochemical properties of the {100}-faceted iron pyrite single crystal electrodes. (a) $J-V$ characteristics for the champion electrode under dark and 1 sun illumination, using 4 M HI/1 M CaI_2/0.05 M I_2 as the aqueous electrolyte vs 20 mM:20 mM $CoCp_2^{0/+}$/1 M TBAP in acetonitrile, as the nonaqueous electrolyte. (b) V_{OC} under 1 sun illumination as a function of redox potential for two representative pyrite electrodes using various redox couples in aqueous and nonaqueous electrolytes. Aqueous redox couples: 20 mM:2 mM $Ru(NH_3)_6^{2+/3+}$/0.5 M H_2SO_4, 10 mM:1 mM $Fe(CN)_6^{4-/3-}$/0.1 M K_2SO_4, 20 mM:2 mM $Fe^{2+/3+}$/0.1 M H_2SO_4, and 25 mM:2.5 mM $Fe(phen)_3^{2+/3+}$/1 M H_2SO_4. Nonaqueous redox couples: 20 mM:2 mM of $CoCp_2{}^*{}^{0/+}$, $CoCp_2^{0/+}$, $DFc^{0/+}$ and $Fc^{0/+}$ in 0.1 TBAP/acetonitrile. Both electrodes were measured using $Fc^{0/+}$ in 0.1 TBAP/acetonitrile as the redox couple to demonstrate their similarities.

a direct ligand field interaction with the surface, which could reduce recombination at the semiconductor/electrolyte interface.[23,65,66] The favorable interaction of I^-/I_2 redox couple with the surface may also be supported by the outstanding stability of iron pyrite PEC cells and high electrocatalytic activity of pyrite compounds for the iodine/iodide reaction.[28,65−68] In such a case, inner-sphere electron transfer explains the observed larger photocurrents. On the other hand, the improvement in V_{OC} observed in the nonaqueous aprotic electrolyte could originate from the suppression of unwanted corrosion reactions usually associated with aqueous and oxygenated electrolytes.[69,70] We measured the $J-V$ characteristics of pyrite single crystal electrodes under 1 sun illumination, from which we observed similar values for V_{OC} and fill factors in comparison to our champion electrode, but lower conversion efficiencies due to significantly lower J_{SC}. Overall, the dark $J-V$ characteristics of the pyrite single crystal electrodes are very reminiscent of a heavily doped semiconductor, in that there is a lack of rectifying behavior (Figure 5a). Together with the low V_{OC} and fill factor under illumination, the $J-V$ characteristics are suggestive of large forward conduction band electron tunneling currents or thermionic emission across the junction barrier.

We further investigated the PEC properties of the pyrite single crystal electrodes using a variety of redox couples that span a wide potential window. From this study, we found that in comparison to the maximum achievable V_{OC} based on theoretical band gap, the photovoltage remains constant in both aqueous and nonaqueous aprotic solvents, regardless of the redox couple potential (Figure 5b). Such behavior is characteristic of Fermi level pinning, where the Fermi level is pinned at the surface due to a large density of surface defect states, rendering the band bending in the semiconductor insensitive to the redox couple potential.[71] The charge or discharge of the surface states as they equilibrate with the chemical potential of the redox couples "buffers" changes in the barrier height and results in the unpinning of the energy bands due to changes in surface charge density. Therefore, the energy band shift caused by equilibration to the redox couple potentials can be used to estimate the density of surface states (N_{SS}) based on the relationship $N_{SS} = \Delta Q_{SS}/e = C_{dl}\cdot\Delta V_{EB}/e$, where ΔQ_{SS} is the change in surface charge, C_{dl} is the double layer capacitance, ΔV_{EB} is the potential shift of the energy bands, and e is the elemental charge.[72−74] Since the potential shift in aqueous electrolytes is limited by the water potential window, we used the nonaqueous redox couple potential window (2 V) in which we observed a "fixed" V_{OC} (Fermi level pinning) (Figure 5b, blue squares) as the potential shift ΔV_{EB} (= 2 V). Then, assuming a typical double layer capacitance of $C_{dl} \sim 10^{-5}$ F/cm^2, we obtained $N_{SS} \sim 1.3 \times 10^{14}$ cm^{-2}. This density of surface states should be considered as a lower bound estimate. Since N_{SS} has the same order of magnitude as the density of Fe atoms on a {100} surface ($\sim 7 \times 10^{14}$ cm^{-2}), it suggests that the origin of the surface states is intrinsic to the reduced coordination of the outermost surface. Similar large energy band shifts and density of surface states have been observed for RuS_2 with the pyrite structure type.[74]

It is important to clarify that the observation of Fermi level pinning will not necessarily be the explanation for the low photovoltage and photoconversion efficiency of pyrite single crystals, since this explanation will be dependent on the resulting charge neutrality condition and barrier height. It has been well documented that there are various mechanisms that can limit the V_{OC} of a liquid junction solar cell even in the presence of Fermi level pinning.[39] Therefore, we proceed to characterize the energetic position of the surface Fermi level in order to assess the impact of Fermi level pinning on the pyrite single crystal performance.

Energetic Position of the Surface Fermi Level. We characterized the energetic position at which the surface Fermi level is pinned relative to the energy bands in the pyrite single crystals using Ultraviolet and X-ray photoelectron spectroscopy (UPS and XPS, respectively) and Kelvin force microscopy (KFM). Figure 6a shows the valence band UP spectrum for a {100}-faceted iron pyrite single crystal after electrochemical cleaning using He I (21.2 eV photon energy) as UV light source (see Supporting Information for details). A piece of platinum foil was used to calibrate and shift binding energies so that the Fermi level in the UP spectra lies at 0 eV. The blue curve in Figure 6b shows that the valence band edge of the FeS_2 sample lies at 0 eV, showing that the FeS_2 valence band maximum lies at the Fermi level. In comparison, no difference was observed for the valence band maximum position with respect to the surface Fermi level after HNA etching (Figure

dx.doi.org/10.1021/ja509142w | J. Am. Chem. Soc. 2014, 136, 17163−17179

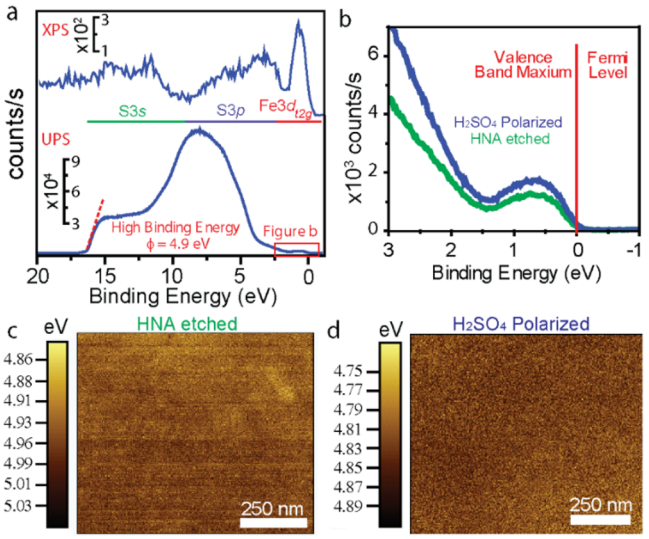

Figure 6. Surface Fermi level and work function characterization of the {100}-faceted pyrite single crystals. (a) Ultraviolet (Hel I, excitation energy of 21.2 eV) and X-ray photoelectron spectra of the valence band for an electrochemically cleaned pyrite single crystal. (b) Zoom in for the surface Fermi level energy region (blue curve) in comparison with an HNA etched (green curve) iron pyrite single crystal. Kelvin force microscopy (KFM) contact potential image for the surface of (c) an HNA etched and (d) an electrochemically cleaned pyrite single crystal.

6b, green curve). The location of the valence band maximum, together with the PEC measurements (Figure 5b), suggests that the surface Fermi level of {100}-faceted iron pyrite is intrinsically pinned at the valence band edge due to a high density of acceptor-like surface states. A work function (ϕ) of 4.9 ± 0.1 eV was obtained from the high binding energy cutoff (Figure 6a). We also used the corresponding valence band XP spectrum to corroborate our valence band maximum assignment in the UP spectrum. The XP spectrum show three distinguishable peaks that can be assigned, using ligand field theory, to the pyrite Fe $3dt_{2g}$, S $3p$, and S $2s$ orbitals resulting from octahedrally coordinated Fe with the sulfur dumbbells.[29] The difference in intensity between UPS and XPS for the Fe $3dt_{2g}$ peak is due to the variation in the total atomic ionization cross-section with photon energy.[29,75]

To corroborate the validity of the UPS results under inert atmosphere conditions, we used KFM measurements to determine the work function of various pyrite single crystals under argon (see Supporting Information for details). Figure 6c,d show the surface potential for a representative pyrite single crystal after HNA etching and electrochemical cleaning. The corresponding surface potential image shows an average work function of 4.9 ± 0.1 eV (Figure 6c) and 4.8 ± 0.1 eV (Figure 6d), respectively. By averaging a total of 36 measurements taken from different areas of the surfaces of 10 pyrite single crystals pretreated by HNA etching, we found an average work function of 4.9 ± 0.1 eV. The average work function of three pyrite single crystals after electrochemical cleaning shows no statistical difference in work function in comparison with HNA etching. The agreement between the work function determined from UPS and KFM confirms that the surface Fermi level observed by UPS is a valid representation of the energetic position at which the band bending appears to be "fixed" in the PEC measurements.

Surface Chemical Species Characterization. To gain further chemical insights about the surface of iron pyrite we performed angle-resolved XPS (AR-XPS) measurements of the sulfur $2p$ peak for the electrochemically cleaned pyrite single crystals (see Supporting Information for details). Through the deconvolution of S $2p$ into its specific constituents insights can

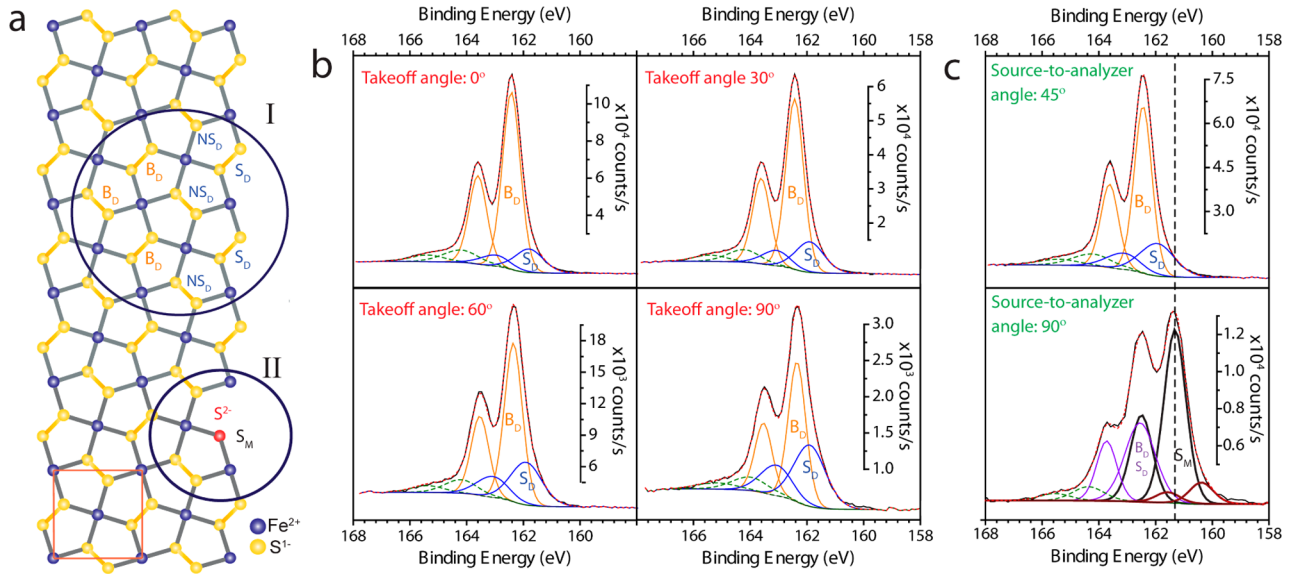

Figure 7. Surface sulfur species for the {100}-faceted iron pyrite single crystals. (a) Schematic representation of a cleaved {100} iron pyrite surface (modeled after Bronold et al.,[35] and Andersson et al.[77]). Circle I shows the intrinsic outermost surface (S_D), near-surface (NS_D) and bulk-like (B_D) disulfide (S_2^{2-}) species. Circle II shows a representations of the sulfur monomer (S^{2-}) species resulting from sulfur vacancies (S_M). (b) AR-XPS of S $2p$ peak for an electrochemically cleaned iron pyrite single crystal taken at takeoff angles of 0°, 30°, 60°, and 90° using a source-to-analyzer angle geometry (α) of 45° and an acceptance angle of ~60°. (c) S $2p$ peak comparison between XP spectrometers with an (α) geometry of 45° (45° takeoff angle, ~60° acceptance angle) and 90° (45° takeoff angle, ~4° acceptance angle). All measurements were taken using an Al Kα source and peaks were fitted using doublets with a 1:0.5 ($p_{3/2}$:$p_{1/2}$) area ratio, 1.18 eV apart, and with the same FWHM.

dx.doi.org/10.1021/ja509142w | J. Am. Chem. Soc. 2014, 136, 17163−17179

be gathered about coordination environment, oxidation state, and charge distributions (Figure 7a) due to different core-level energy shifts (CLS) of surface sulfur species relative to bulk.[35,76−78] Figure 7b shows the AR-XPS results at takeoff angles of 0°, 30°, 60°, and 90° using a source-to-analyzer angle geometry (α) of 45° and an acceptance angle of ∼60°. The binding energy (BE) region plotted in Figure 7b was selected for the purpose of clarity, and no other S 2*p* peaks, such as for sulfate species, were observed in our measurements. At all takeoff angles we observed two different species in the S $2p_{3/2}$ spectra with BEs of 162.4 eV (orange doublet) and 161.8 eV (blue doublet). These S $2p_{3/2}$ species can be attributed to intrinsic bulk-like disulfides (B_D) and surface disulfides (NS_D and S_D) on the {100} surface of iron pyrite (Figure 7a, circle I).[35,76] Additionally, a high BE shoulder feature (green doublet) was observed at 164.2−165.4 eV; given that its relative intensity does not change with takeoff angles we interpret this feature to be caused by a core hole effect following a recent report.[79] As the takeoff angle increases to 90°, the relative intensity of the 161.8 eV S $2p_{3/2}$ peak increased significantly. Since the sampling depth (d) decreases with takeoff angle (θ) based on the equation: $d = \lambda_{IMFP} \cos \theta$, where λ_{IMFP} is the inelastic mean *free* path (for Al Kα photon energy, the λ_{IMFP} for sulfur is about 2.67 nm[80]), the increase in relative intensity with takeoff angle suggest that these species are located near the outermost surface. We estimate that for an analyzer with ∼60° acceptance angle, at a takeoff angle of 90° the sampling depth range is $d \leq$ 1.34 nm or ≤2.5 unit cells from the surface.

When investigating the surface S2*p* species using an XP spectrometer with α = 90° geometry and acceptance angle of ∼4°, we observed an S $2p_{3/2}$ peak at 161.3 eV and a small shoulder peak at 160.9 eV (Figure 7c). Furthermore, the S $2p_{3/2}$ bulk disulfide peak at a 162.5 eV BE could only be fit with a FWHM wider than its corresponding S $2p_{1/2}$ doublet pair, indicating that the observed surface disulfide species with an S $2p_{3/2}$ BE of 161.9 eV when using an XP spectrometer with α = 45° geometry is still present but cannot be fully resolved. The appearance of other chemical species at α = 90° geometry in comparison with α = 45° geometry is due to the higher sensitivity of the relative intensity to the angular asymmetry of photoemitted S 2*p* electrons. The effects of the angular distribution on the relative intensity of chemical species can be illustrated by the photoionization cross-section (σ) equation in the dipole approximation at a fixed source energy:[81]

$$\sigma = \frac{\sigma_T}{4\pi}\left[1 - \frac{1}{4}\beta(3\cos^2\alpha - 1)\right] \quad (5)$$

where β is the asymmetry factor. Due to the dependence of σ on α, at α = 90° geometry, the relative intensity of S 2*p* chemical species will be most influenced by the β differences among species.[81] Chemical species at the outermost crystal surface can have different β terms due to differences in chemical coordination or screening of photoemitted electrons.[82,83]

The 161.3 eV S $2p_{3/2}$ species seen at α = 90° geometry have only been previously observed for cleaved {100}-iron pyrite single crystals when measuring at low synchrotron photon energies of 200−245 eV where $\lambda_{IMFP} \approx$ 0.4 nm.[35,77,84] Therefore, there is a general agreement that these sulfur species are located at the outermost atomic plane. However, due to the large 1.2 eV CLS from bulk disulfides, there has been disagreement on the interpretation of their chemical identity. To experimentally differentiate if the 1.2 eV CLS is caused by a change in oxidation state (sulfur monomer, S^{2-})[77,79] or by the surface charge distribution resulting from the observed Fermi level pinning,[35] we compared the S 2*p* peak for iron pyrite against metallic cobalt pyrite (see Figure S4 in the Supporting Information). Since the 1.2 eV CLS sulfur species were also observed in cobalt pyrite despite being a metal, we assigned the 161.3 eV S $2p_{3/2}$ peak to sulfur monomers (S^{2-}) caused by surface vacancies (S_M, Figure 7a, circle II). Furthermore, a small S $2p_{3/2}$ shoulder peak at low BEs was also observed in cobalt pyrite; thus, the 160.9 eV S $2p_{3/2}$ shoulder peak for iron pyrite can be attributed to a more reactive outermost surface species.[77] In contrast, the 161.8 eV S $2p_{3/2}$ peak observed at α = 45° geometry was the only species absent in cobalt pyrite. Considering that cobalt pyrite is a metal, the presence of this peak in iron pyrite suggest that the 0.6 eV CLS of the surface disulfide species (161.8 eV S $2p_{3/2}$ peak) is caused by the charge distribution in the space charge region (band bending);[85,86] therefore, the CLS should correspond to the difference in energy between the bulk and surface Fermi level (barrier height). Utilizing the characterized *free* carrier concentration of 1×10^{15} cm^{-3}, band gap of ∼0.8 eV, and surface Fermi level at the valence band edge, the total barrier height (Ψ_T) for the iron pyrite single crystals was calculated to be $\Psi_T \approx$ 0.6 eV, which is in good agreement with the observed CLS for the surface disulfides. This agreement suggests that most of the charge in the space charge region is localized near the surface ($<3\cdot\lambda_{IMFP}$ = 5.34 nm), in other words most of the band bending occurs near the surface. At the moment, this conclusion is unexpected since a low *free* carrier concentration would suggest a wide space charge region. However, as we will discuss later, this is consistent with the semiconducting space charge region properties of iron pyrite when considering the impact of a high density of donor states on the charge distribution of the space charge region. Furthermore, the analysis of S 2*p* XPS for the electrochemically cleaned pyrite single crystals suggests that the surface states responsible for the strong Fermi level pinning originate from the intrinsic reduced coordination environment of the outermost surface atoms, as hypothesized for the {100} surface of iron pyrite.[35] Therefore, the outermost surface (S_A in Figure 7, Circle I) can be considered to have a different electronic structure than bulk, while the chemical species such as sulfur monomers (S_M in Figure 7, Circle II) can be consider as point defects.[31]

Here we need to emphasize that Fermi level pinning cannot explain the low photoconversion performance of the pyrite single crystals. On the basis of the agreement between the UPS and KFM results for the location of the surface Fermi level, we demonstrated that the observed Fermi level pinning in the PEC measurements is due to a high density of intrinsic surface states located near the valence band edge. The equilibration between bulk and surface states results in a charge neutrality condition that pins the surface Fermi level at the valence band edge on the {100} surface. The resulting band bending will have a large barrier height and should lead to a V_{OC} close to the largest achievable based on the bulk Fermi level and band gap. Consequently, the observation of Fermi level pinning due to a high density of surface states does not explain the low V_{OC} and poor photoconversion efficiency of the pyrite single crystal electrodes. It should be emphasized the possible detrimental effects that such states could have in surface recombination cannot be fully dismissed since we would need to know their precise energy distribution and occupancy. However, we must consider the high density of bulk deep states, on the order of 10^{19}−10^{20} cm^{-3}, as a more reasonable explanation for the low

V_{OC}, and poor photoconversion efficiency. Furthermore, as we learned from the AR-XPS analysis of S 2*p* peak the band bending in the space charge region appears to occur mostly near the surface. Therefore, we must investigate the effects of bulk deep donor state ionization on the overall characteristics of the space charge region.

Electrochemical Impedance Spectroscopy Circuit Model Fitting. We studied the effects of the bulk and surface defects in the space charge region of the {100}-faceted iron pyrite electrodes through electrochemical impedance spectroscopy (EIS). The EIS was carried out in a three-electrode configuration with a home-built Ag/0.01 M $AgClO_4$ reference electrode using only the supporting electrolyte 0.1 M TBAP/acetonitrile under an Ar atmosphere, to reduce the complexity of corrosion reactions that readily occur in aqueous electrolytes and under oxygenated atmosphere.[60,61] Figure 8a presents a

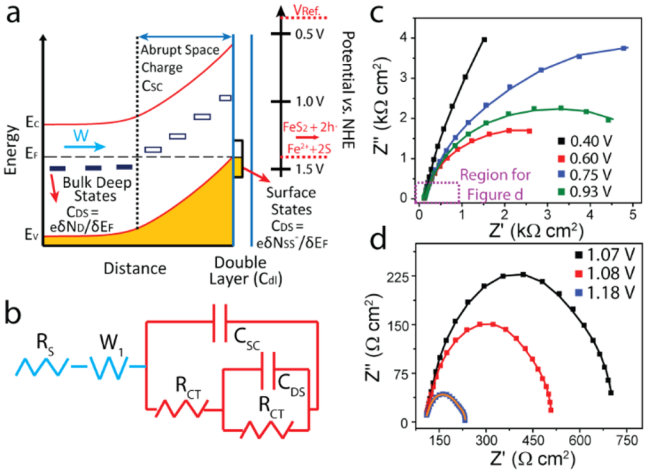

Figure 8. Electrochemical impedance spectroscopy (EIS) of a representative {100}-faceted iron pyrite single crystal electrode. (a) Hypothetical band bending scheme deduced from the electrical transport, photoelectrochemical and surface characterization measurements so far. This scheme is placed in an electrochemical scale relative to the potential of the home-built Ag/0.01 M $AgClO_4$ reference electrode ($V_{ref.}$) and the anodic dissolution potential of iron pyrite. (b) Proposed simplified equivalent circuit model for the medium to low frequency range of 2.2 kHz to 1 Hz. (c) Nyquist impedance plots using 0.1 TBAP/acetonitrile as electrolyte for the potential bias (DC) of 0.40 V (black squares), 0.60 V (red squares), 0.75 V (blue squares), and 0.93 V (green squares) vs $Fc^{0/+}$; (d) and potential bias (DC) of 1.07 V (black squares), 1.08 V (red squares), and 1.18 V (blue squares) vs $Fc^{0/+}$. The corresponding circuit model fitting results are plotted as solid lines.

hypothetical band bending scheme for the iron pyrite electrode/electrolyte interface generated from the experimental evidence discussed thus far. In this scheme, we describe the bulk as *n*-type due to the presence of deep donor states (N_D), and the surface to be pinned near the valence band edge due to a high density of acceptor defect states (N_{SS}). In the TBAP/acetonitrile electrolyte, the surface acceptor states equilibrate with the anodic dissolution potential of iron pyrite, pinning the position of the conduction and valence bands. In the three-electrode EIS measurements, the band bending at zero applied (DC) bias is in accumulation, because the reference electrode potential ($V_{ref.}$) is located above the conduction band of iron pyrite (Figure 8a). In accumulation, electrons are trapped/localized in the deep donor states (N_D) and ionized surface acceptor states (N_{SS}^-) at steady-state. Under forward bias the surface Fermi level moves from the conduction band toward the valence band, which results in the ionization of N_D and repopulation of N_{SS}^-. This charge/discharge of defect states is a faradaic process that can be modeled analogously as a pseudocapacitor, which enables the characterization of the density of states (DOS) for N_D and N_{SS}^- from EIS measurements using circuit model fitting.[87] On the basis of this hypothesis, a complete analogous circuit model was constructed (see Figure S5 in the Supporting Information) to explain the electrochemical impedance of the pyrite electrodes and further characterize the energetic distribution of defect states in the space charge region and interface.

Figure 8b shows our simplified circuit model for the medium to low frequency EIS response of the pyrite single crystal electrodes, which is composed of a pseudocapacitive-like combination of the space charge region capacitance (C_{SC}) and defect states faradaic capacitance (C_{DS}) (colored in red). C_{SC} originates from the charge density and electric field distribution within the abrupt space charge region, while the pseudocapacitor-like C_{DS} originates from the charge transfer process associated with the charge/discharge of defect states. Since electrons can be localized/trapped in singly occupied deep donor states (N_D) or ionized surface acceptor states (N_{SS}^-), the circuit element C_{DS} would be influenced by both. In a sense, the proposed circuit model describes the coexistence of double layer capacitance and pseudocapacitance. In addition, this model contains a finite Warburg element (W_1) that serves as a transmission line describing a bulk transport/recombination resistance (see Figure S5 in the Supporting Information for more discussion on the origin of W_1).[88,89] Figure 8c,d shows the Nyquist plots for a representative pyrite electrode under dark conditions, in the range of 2.2 kHz to 1 Hz under various applied voltages. Solid lines show the fitting of the experimental data to the proposed circuit model. It is clear that they describe the EIS data quite well within the large potential window used in the experiments. Since this proposed circuit model was based on an experimental understanding of the {100}-faceted iron pyrite single crystals and balances a reasonable physical description with the least number of variables, we believe this model is valid for the EIS study of pyrite single crystals. Next we proceed with the analysis of the fitting parameters obtained using this analogous circuit model, which are then critically evaluated in the context of our experimental electrical transport and surface characterization measurements, and theoretically using the Poisson equation.

Fitting Results of Electrochemical Impedance Spectroscopy. We first evaluated the circuit model fitting results for C_{SC}, using a plot of $1/C_{SC}^2$ vs V, commonly referred to as the Mott–Schottky plot. Figure 9a (solid black circles) shows the Mott–Schottky plot for a representative pyrite single crystal, in the potential window of 0.30–0.86 V vs $Fc^{0/+}$, from which we observed a linear region with a positive slope. Following the classical Mott–Schottky relationship,

$$\frac{1}{C_{SC}^2} = \frac{2}{e\varepsilon_0\varepsilon_S N_D}(V - E_{FB}) \tag{6}$$

we found that the slope is consistent with the depletion region capacitance of an *n*-type iron pyrite semiconductor. By linear extrapolation, we obtained a concentration of ionized donors $N_D = 2.1 \times 10^{20}$ cm^{-3} and an *x*-intercept, which we will refer to as the apparent flat band potential (E_{FB}^*) of $E_{FB}^* = 0.64$ V vs $Fc^{0/+}$. Under the classical Mott–Schottky relationship

dx.doi.org/10.1021/ja509142w | J. Am. Chem. Soc. 2014, 136, 17163–17179

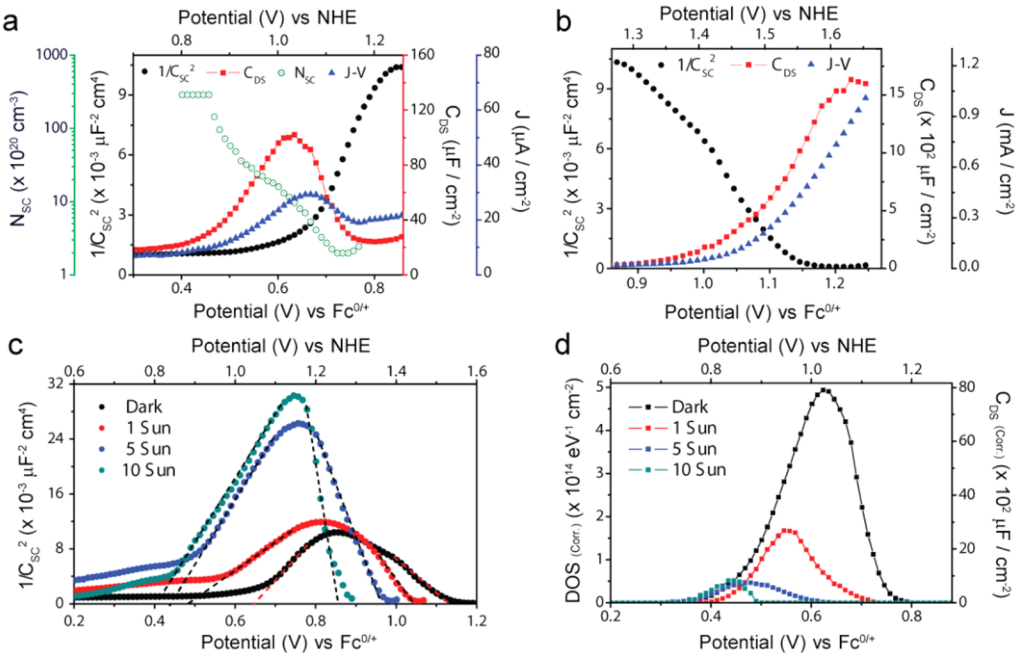

Figure 9. EIS fitting results for a representative {100}-faceted pyrite single crystal electrode. $1/C_{SC}^2$ (solid black circles), C_{DS} (red squares) values, and *J-V* curve (blue triangles) obtained under dark condition for the potential window vs $Fc^{0/+}$, of (a) 0.3−0.86 V (depletion region) and (b) 0.86−1.26 V (inversion region). The apparent charge density in the abrupt space charge region (N_{SC}) (green open circles) was included for the potential window of (a) 0.3−0.86 V vs $Fc^{0/+}$, as a further comparison between $1/C_{SC}^2$ and C_{DS}. Note the large difference in scale for *J*−*V* and C_{DS} in panel b. (c) Plot of C_{SC}^2 vs *V* plot under different illumination conditions: dark (black circles), 1 sun (red circles), 5 sun (blue circles), and 10 sun (cyan circles) illumination. (d) Corresponding density of states calculated from the background corrected values of C_{DS}, for the aforementioned illumination conditions.

assumption, the obtained ionized donor concentration should correspond to shallow dopants and appears to contradict the *free* carrier concentration obtained from the room temperature Hall effect measurements (Figure 2c). However, when considering the large density of deep donor states (N_D = (7.6 ± 3.3) × 10^{19} cm^{-3}) obtained by combining the large thermal activation energy (from temperature-resistivity measurements) with the *free* carrier concentration, a good agreement was found with the ionized donor concentration in the space charge region. Similarly, the agreement can be demonstrated by calculating the *free* carrier concentration based on the assumption that the ionized donor concentration corresponds to the total deep donor concentration (see Figure S7 in the Supporting Information for a graphical solution).

To demonstrate that the Mott−Schottky relationship is still valid for determining the concentration of deep donor states, we solved the corresponding Poisson equation for pyrite single crystals to determine the dependence of capacitance vs applied voltage in the Supporting Information. We found that the corresponding Mott−Schottky relationship for a high density of deep donor states (obeying a Fermi−Dirac distribution (eq 2)) has the general form:

$$\frac{1}{C_{SC}^2} = \frac{2}{e\varepsilon_0\varepsilon_S N_D}(V - (E_D - \ln(1/g_D)k_BT)) \quad (7)$$

where N_D is the concentration of deep donor states, g_D is the state degeneracy, and $E_D - \ln(1/g_D)k_BT$ is the apparent flat band potential (E_{FB}*) discussed above. From this modified Mott−Schottky equation (eq 7), a plot of $1/C_{SC}^2$ vs *V* still results in a linear region with a slope that is dependent on the deep donor concentration and carrier type, but the intercept now corresponds to the half occupancy ($F_{1/2}$) of the deep donor band based on eq 2 (see Figures S8 and S9 in the Supporting Information for a numerical simulation of $1/C_{SC}^2$ vs *V*).

We will now compare our circuit model fitting results for the defect states faradaic capacitance (C_{DS}) with $1/C_{SC}^2$ vs *V*. Figure 9a (red squares) shows a plot of C_{DS} vs *V* where a wide peak centered at about 0.64 V vs $Fc^{0/+}$ can be observed. The energetic distribution of the density of states ($g(E_F)$) or DOS for the defect states is related to C_{DS} by[87,90]

$$C_{DS}(V) = eg(E_F) = e\delta N_{DS}(E_F)/\delta E_F \quad (8)$$

where N_{DS} represents the singly occupied donor states (N_D) or ionized surface acceptors states (N_{SS}^-). In accordance with eq 8, and assuming a Fermi−Dirac distribution (eq 2), the observed C_{DS} peak can be attributed to the energetic distribution of localized/trapped electrons in a deep donor state band, which in our case reaches a maximum DOS of 6.3 × 10^{14} eV^{-1} cm^{-2}. Therefore, it is not surprising that the peak maximum coincides with the apparent flat band potential, since both correspond to the potential at which the deep donor band is half-occupied ($F_{1/2}$). We observed further agreement between C_{DS} and C_{SC} when calculating the apparent charge density (N_{SC}) in the abrupt space charge region as a function of the applied voltage:[91]

$$N_{SC}(V) = -\frac{C_{SC}^2}{e\varepsilon_0\varepsilon_S(\delta C_{SC}/\delta V)} = -\frac{2}{e\varepsilon_0\varepsilon_S}\cdot\frac{\delta(1/C_{SC}^2)}{\delta V} \quad (9)$$

In the presence of deep donor states and negligible shallow states, $N_{SC}(V)$ is dependent on both the ionized and singly occupied deep donor states (N_D^+ and N_D, respectively). When the abrupt space charge depth (X_D) is equal or smaller than the Debye length (L_D) for the deep donor states [$N_D(x)$ band

dx.doi.org/10.1021/ja509142w | J. Am. Chem. Soc. 2014, 136, 17163−17179

falloff], the apparent charge density reaches a maximum [N_{SC}(max)] given by the equation:[92,93]

$$N_{SC}(\max) \cong N_D^+(\text{bulk}) + \frac{W_N}{L_D}\cdot N_D(\text{bulk}) \quad (10)$$

where W_N is the width of the nonconstant space charge region (see detailed description of the nonconstant space charge region in the Discussion section). Note that in eq 10 the space charge region was modeled as a double sided junction between the nonconstant region and abrupt region, to account for the screening of the nonconstant region by the large charge density distribution [$\rho(x)$] of the abrupt region. As the abrupt space charge depth increases and the deep donor states become ionized, the charge density will decrease, reaching a minimum value of $N_{SC}(\min) = N_D^+ = N_D(\text{bulk})$ when the deep donor state band becomes fully ionized.[89,90] Indeed, the N_{SC} vs V plot (Figure 9a, green circles) shows that as the electrode is polarized toward anodic potentials, the apparent charge density drops across the defect band, indicating the ionization of localized electrons in the abrupt space charge region and confirming our results for C_{DS} vs V. The corresponding $J-V$ curve (Figure 9a, blue triangles) also shows a peak current in this potential window. Since the electrolyte is only supporting electrolyte (0.1 M TBAP) in acetonitrile, we can associate these currents with the ionization of the deep donor defect band. Therefore, the $J-V$ curve provides further supporting evidence for the C_{SC} and C_{DS} results obtained by circuit model fitting.

Figure 9b shows the evolution of $1/C_{SC}^2$, C_{DS}, and $J-V$ at a higher anodic potential window of 0.86−1.25 V vs $Fc^{0/+}$. First, we observed a slope with opposite sign in the $1/C_{SC}^2$ vs V plot (solid black circles), caused by an increase in the space charge capacitance. As an initial hypothesis, we associate this behavior to the accumulation of minority carriers (holes) at the semiconductor/electrolyte interface. Under further scrutiny, we notice that the $1/C_{SC}^2$ dependence with voltage does not follow the sharp slope change predicted for the inversion region in the classical semiconductor treatments. Such discrepancy is due to the high density of deep donor states, which is comparable to or exceeding that of the reported effective density of states at the valence band edge (N_V) of iron pyrite ($N_V \approx 8.5 \times 10^{19}$ cm^{-3}).[3] In section II.7 of the Supporting Information, we solve the corresponding Poisson equation and demonstrate graphically (Figure S7) that in the case where $N_{DS} \geq N_V$, the charge, and consequently the capacitance of the space charge region, reaches only a weak inversion dependence for Fermi level potentials within the band gap. As the Fermi level moves beyond the valence band edge, the population of holes at the valence band can no longer be described by the Maxwell−Boltzmann approximation for the distribution of holes. Consequently, we expect that the $1/C_{SC}^2$ vs V will change from the linear dependence of the weak inversion to a sharper decrease in $1/C_{SC}^2$ as the Fermi level transitions into the valence band (see Figure S9 in the Supporting Information for simulated plots of $1/C_{SC}^2$ vs V). Indeed, from Figure 9b, we can observe a change in the dependence of $1/C_{SC}^2$ vs V at about 0.99 V vs $Fc^{0/+}$, a potential that can be used as an estimate of the valence band edge. On the basis of eq 7, by subtracting E_{FB}^* = 0.64 V vs $Fc^{0/+}$, we can relate the estimated valence band edge potential to the half-occupancy of the deep donor band. Then, using $g_D = 4$ (following Bronold et al.[37]) and E_D from the high temperature resistivity measurements, the band gap was estimated to be $E_g = 0.84 \pm 0.01$ eV, which is in agreement with the optoelectronic band gap obtained from SPV measurements for the electrochemically cleaned pyrite single crystal (Figure 3d).

To discuss the fitting results for C_{DS} vs V in the inversion region (Figure 9b red squares), we must recall our Fermi level pinning analysis, from which we inferred the presence of a high density of surface acceptor states located near the valence band edge. Therefore, we expect that as the Fermi level moves toward the valence band, C_{DS} will increase accordingly with the ionization of the surface acceptor states. In fact, the C_{DS} vs V plot shows an increase starting at about 0.99 V vs $Fc^{0/+}$ that is accompanied by a large increase in anodic current in the $J-V$ curve (Figure 9b blue triangles). Under the assumption of a Fermi−Dirac distribution and following eq 8, we can explain the increase in C_{DS} and $J-V$ to be caused by the repopulation of ionized surface acceptor states (N_{SS}^-), which then serve as hole-mediating sites. The C_{DS} vs V trace appears to reach a maximum at ∼1.22−1.25 V vs $Fc^{0/+}$, but due to an increasingly large shunting resistance, we are unable to further characterize this feature. We hypothesize that by applying such large anodic potentials, we are tuning the surface Fermi level into the valence band and significantly increasing the population of holes, enabling a direct charge transfer pathway. Despite this limitation, we can still use eq 8 to estimate the area density of surface state (N_{SS}) by fitting C_{DS} (Figure 9b red squares) to a Gaussian distribution (Figure S6 in the Supporting Information), from which N_{SS} is estimated to be 2.6×10^{15} cm^{-2}. This estimated area density of surface states is similar to the value of $N_{SS} = 1.4 \times 10^{15}$ cm^{-2} predicted by ligand field theory (LFT) for an intrinsic {100} surface (2 surface states per Fe atom).[35]

According to the discussion of $1/C_{SC}^2$ vs V in the inversion region, the position of the surface acceptor band relative to the energy bands can be determined utilizing 0.99 V vs $Fc^{0/+}$ as an estimate of the valence band edge. The comparison of C_{DS} (red squares) with $1/C_{SC}^2$ (black circles) in Figure 9b shows that the surface acceptor band maximum lies within the valence band and tails-off into the band gap to ∼100 mV from the estimated valence band edge. Given that the surface Fermi level of pyrite single crystals is intrinsically pinned at the valence band edge, the surface acceptor band is expected to be mostly occupied at intrinsic steady-state equilibrium conditions. The results for the surface acceptor states are in good agreement with the characterized deep donor concentration and observed strong Fermi level pinning. This agreement can be demonstrated using the classical charge neutrality conditions[48] to estimate the minimum density of surface states for Fermi level pinning. For the obtained $N_D \sim 10^{20}$ cm^{-3}, the estimated minimum density of occupied surface states is ∼10^{15} cm^{-2}, thus the charge neutrality condition also supports the results for area density, energy distribution, and occupancy of the surface acceptor states.

EIS Fitting Results under Different Illuminations Intensities. We also investigated the effect of illumination intensity on the fitted parameters of C_{SC} and C_{DS} for the {100}-faceted pyrite single crystal electrodes. Figure 9c shows $1/C_{SC}^2$ vs V, for dark, 1 sun, 5 sun, and 10 sun illumination conditions, where a peak feature that shifts toward higher cathodic potentials with increasing illumination intensity is always observed. Similarly to the discussion for dark condition, the positive slope corresponds to an n-type depletion region, followed by a negative slope corresponding to a carrier inversion region for all illuminated measurements. Therefore, by extrapolating the linear region with positive slope, we can

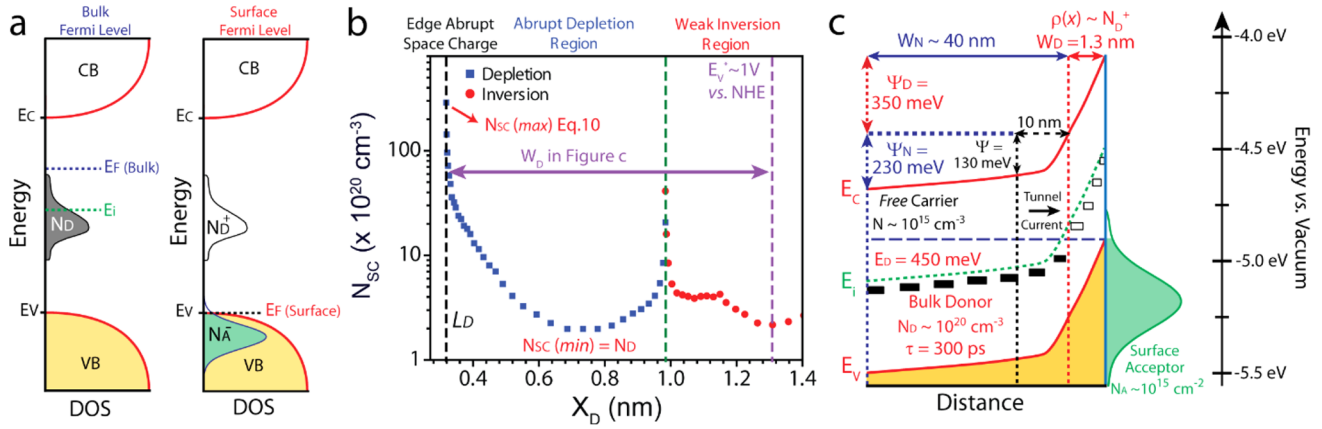

Figure 10. Space charge region properties of the iron pyrite single crystals. (a) Occupancy of the deep donor (N_D) density of states (DOS) relative to the bulk and surface Fermi level, as determined from the EIS measurements. Surface states (N_A) are plotted for the purpose of illustrating their occupancy under surface Fermi level pinning. (b) Experimental profile for the apparent charge density in the abrupt space charge region (N_{SC}) as a function of the variable abrupt space charge depth (X_D), as determined from the fitting results for C_{SC} vs V under dark conditions. The total width of the abrupt space charge region (W_D) under surface Fermi level pinning condition is shown using a purple double-sided arrow and was calculated using the estimated valence band edge potential (E_V*). (c) Proposed energy band scheme for {100}-faceted iron pyrite single crystal with various values determined experimentally herein.

compare the changes in ionized donor concentration and apparent flat band potential (x-intercept). The ionized donor concentration remains fairly constant as a function of illumination, changing from 2.1 × 10^{20} cm^{-3} for dark, to 3.0 × 10^{20} cm^{-3} for 1 sun, and 1.4 × 10^{20} cm^{-3} for 5 and 10 sun. In contrast, we observed a significant and systematic shift in the apparent flat band potential, changing from 0.64 V for dark, to 0.49, 0.44, and 0.41 V vs $Fc^{0/+}$, for 1, 5, and 10 sun, respectively. This observed shift in the apparent flat band potential with increasing illumination intensity is consistent with Fermi level pinning.[94,95] This behavior is more commonly known as energy band unpinning, which refers to a shift in the conduction and valence band potentials caused by a change in the interfacial charge density at steady-state equilibrium.[71] Furthermore, we observed that the onset of the inversion region also shifts with increasing illumination intensity and the negative slope evolves from a wide tail under dark condition, to a sharper linear change under 5 and 10 sun illumination (Figure 9c). In addition, the change in the inversion region is accompanied by an earlier onset in cathodic current. All of these observations indicate that the systematic shift of the $1/C_{SC}^2$ vs V peak feature is caused by a cathodic shift of the conduction and valence band potentials. To understand the origin and direction of this potential shift, we need to recall that the surface of iron pyrite is negatively charged under intrinsic equilibrium conditions due to ionized surface acceptor states (N_{SS}^-). The density of ionized surface acceptor states (N_{SS}^-) decrease with increasing illumination intensity due to an increasing surface density of valence band holes (holes quasi-Fermi level lowering). Consequently, the surface charge becomes less negative at steady-state equilibrium conditions with increasing illumination intensity and the energy bands shift toward cathodic potentials due to a less positive double layer charge.[71,96]

Furthermore, we observed a decrease in DOS for the deep donor defect band with increasing illumination intensity. Figure 9d shows the background subtracted DOS (calculated from the results for C_{DS} using eq 8) under different illumination conditions. The observed decrease in DOS with increasing illumination intensity indicates a decrease in the density of singly occupied deep donor states, which is consistent with the photoexcitation of localized/trapped deep donor state electrons. The changes in DOS are accompanied by a systematic cathodic potential shift in the defect band maximum which is consistent with the observed energy band shift in the $1/C_{SC}^2$ vs V results under illumination. We notice that for the measurements under illumination the voltage of the defect state maximum corresponds to the onset potential for the linear region in the $1/C_{SC}^2$ vs V, similar to the correspondence seen under dark conditions. In general, the results for the donor defect band under illumination conditions are in agreement with the sub-band gap absorption observed in the UV−vis-NIR measurements (Figure 3a).

■ DISCUSSION

With the use of electrical transport, optical spectroscopy, surface photovoltage, UV and X-ray photoelectron spectroscopy, photoelectrochemical, and electrochemical impedance measurements, we have characterized the properties of intrinsic bulk deep donor states and surface acceptor states in pyrite single crystals (Figure 10a). Now, we can holistically evaluate the impact of these defect states on the space charge properties, which will allow us to understand the low solar conversion efficiency of n-type pyrite single crystal based solar cells.

Effects of Surface Defect States. We will first discuss the effect of surface states on the space charge region, and interfacial properties of iron pyrite. The UPS, XPS, and KFM analyses show that the surface Fermi level of the pyrite single crystals is intrinsically pinned near the valence band edge. We can infer based on the PEC and EIS measurements that this is due to the resulting charge neutrality condition caused by the equilibration of the bulk Fermi level with a high density of surface acceptor states. The resulting band bending or barrier height should be large, which should lead to a V_{OC} comparable to the largest achievable based on bulk Fermi level and band gap. From this perspective, the intrinsic Fermi level pinning of the {100} surface of iron pyrite should cause a beneficial buried junction rather than being detrimental and, thus, is not a satisfactory explanation for the low V_{OC} and limited performance of pyrite based solar cells.

dx.doi.org/10.1021/ja509142w | J. Am. Chem. Soc. 2014, 136, 17163−17179

A more thorough evaluation of the impact of surface states on the space charge region needs to consider their contributions to tunneling and recombination. According to the EIS measurements, it seems unlikely that the surface acceptor states responsible for the Fermi level pinning could have a dramatic impact on surface recombination and majority carrier tunneling to result in the low V_{OC} of pyrite single crystals. As shown by the EIS fitting results for C_{DS} vs V (Figure 9b), when the surface Fermi level is near the valence band edge, the acceptor states are mostly occupied (N_A^-) and only a tail of states extends roughly 100 meV into the band gap (see Figure 10a). Under the intrinsic Fermi level pinning, the negatively charged surface states are spatially separated from the positive space charge region and the charge accumulation results in a Schottky buried junction. In this regard, it appears that surface states can actually help to mediate and facilitate the extraction of photogenerated minority carriers across the interface. Therefore, surface recombination caused only by surface states is unlikely to be the main factor limiting the performance of iron pyrite single crystals.

Effects of High-Density Bulk Deep Donor States on the Space Charge Region. On the basis of the results presented herein, a more plausible cause for the low efficiency of pyrite single crystal based solar cells is the presence of a high density of bulk deep donor states. Although the presence of intrinsic bulk deep states in iron pyrite and their possible detrimental effects have been previously theoretically contemplated,[10,37] no direct experimental evidence of their energetic distribution and full assessment of their impacts on the space charge region properties have been reported. Here the electrical transport (Figure 2) and EIS measurements (Figure 9) showed the presence of a high density of deep donor states with N_D = 10^{19}–10^{20} cm^{-3}, which have a wide energy distribution with a band maximum located about midway into the band gap (E_D = 452 ± 12 meV from the conduction band), as illustrated in Figure 10a. However, the large thermal activation energy of E_a = 226 ± 6 meV of these deep donor states results in a bulk *free* carrier concentrations of only $N = 1.1 \times 10^{15}$ cm^{-3}. Since only a small fraction of deep donor states is thermally ionized, it is important to combine Hall effect measurements with electrical transport and capacitance-based measurements such as EIS to determine the bulk donor concentration. Additionally, the observations of low temperature hopping conduction and a Hall coefficient minimum (Figure 2) are in agreement with the wide deep donor state band observed by EIS (Figure 9a), since the presence of localized states near the bulk Fermi level can enable hopping transport without significant changes in *free* carrier concentration.[51,53,56] Reflective pump–probe measurements (Figure 4) revealed ultrafast carrier lifetimes of τ = 300 ps that can be attributed to the high density of bulk deep states. Singly occupied deep donor states (N_D) within the excitation volume under illumination conditions can act as trap centers for photogenerated holes and recombination can proceed by relaxation of conduction band electrons. We found evidence for the partial ionization of the deep donor state band under illumination condition from the EIS analysis (Figure 9c,d), where we observed a change in the steady-state occupancy for the singly occupied deep donor state band. Furthermore, the EIS analysis shows that deep donor states can also be fully ionized within the space charge region under dark condition, given the intrinsic surface Fermi level pinning (Figure 10a). Thus, the ionization of such a wide deep donor band is expected to have a profound effect on the homogeneity of the charge distribution [$\rho(x)$]. Ionized deep donor states (N_D^+) can also contribute to recombination, since they can provide pathways for conduction band electrons to recombine with photogenerated holes by direct relaxation into the valence band or assisted tunneling toward the interface.

To carefully evaluate the impact of the ionization of high-density deep donor states on the space charge width, charge distribution, and barrier height of iron pyrite single crystals, we solved the corresponding Poisson equation for pyrite single crystals using the experimental evidence that we have presented (see Supporting Information for details). Given the effective density of states at the valence band edge of $N_V \approx 8.5 \times 10^{19}$ cm^{-3} for iron pyrite,[3] the high-density deep donor states of $N_D \approx 10^{20}$ cm^{-3} but low *free* electron concentration of $N \approx 10^{15}$ cm^{-3} leads to a very unusual regime between a semiconductor with discrete deep states (N and $N_D \leq N_V$ or N_C) and a degenerate semiconductor (N and $N_D^+ > N_V$ or N_C). The condition $N_D \geq N_V$ implies that for energies within band gap, the concentration of holes is always lower than the concentration of ionized deep donor states N_D^+. Consequently, the charge density distribution [$\rho(x)$] in the space charge region at the intrinsic surface Fermi level will be governed by the ionization of deep donor states. The space charge can be divided into two distinctive regimes: (i) a nonconstant regime in which the charge density follows the ionization of deep donor states [$\rho(x) = N_D^+(x)$] and, (ii) an abrupt regime in which the charge density equals the concentration of deep donor states [$\rho(x) = N_D$]. We discuss these two regimes in detail below:

(i) The nonconstant space charge region can be defined for potentials within bulk Fermi level and the half occupancy ($F_{1/2}$) of the deep donor band (based on eq 2). Hence, the total barrier height [Ψ_N (*total*)] in this region has the general expression Ψ_N (*total*) = $E_{F(bulk)} - (E_D - \ln(1/g_D)k_BT)$, which predicts that Ψ_N (*total*) = 280 ± 10 meV for a singly to triply degenerate state (g_D range of 2–6). Within this region, changes in the Fermi level will cause changes in the density of ionized deep donor states (N_D^+), and thus, the charge density can be described using a Fermi–Dirac distribution (eq 2). As a result, the nonconstant space charge width (W_N) will be thinner than an abrupt space charge region with the same barrier height and a charge density distribution equal to the *free* carrier concentration of $N = 1.1 \times 10^{15}$ cm^{-3}. The nonconstant space charge width was calculated to be W_N = 37 nm using the EIS fitting results for C_{SC} vs V and eq 9 to calculate the maximum charge density within the abrupt space charge region [N_{SC} (max)], and then eq 10 to solve for the W_N (L_D was experimentally obtained from Figure 10b).[92,93] Theoretically, we estimated the W_N to be roughly 70 nm by numerically solving the Poisson equation using the bulk Fermi level as the initial boundary condition (Figure S10 in the Supporting Information). However, considering the classical depletion approximation, using the bulk Fermi level as the initial boundary condition results in an overestimation of the W_N, because it includes the region where *free* electrons contribute to the charge density and electric field. To verify that the differences between the experimental and theoretical value of W_N can be attributed to the depletion approximation, we calculated the Debye length based on the theoretical charge density distribution [$\rho(x) = N_D^+ + N_p - N_e$] when W_N = 37 nm, and subtracted the resulting Debye length (nonconstant space charge region falloff) of 30 nm from the value of W_N obtained from the Poisson equation. The theoretical value for the W_N

from the edge of the nonconstant space charge region is W_N = 40 nm, which is in excellent agreement with the experimental value of W_N. The corresponding barrier height for the refined theoretical W_N value is $\Psi_N = 230 \pm 10$ meV. Furthermore, we found from the Poisson equation results for the nonconstant space charge region that 130 meV of this barrier height (Ψ_N) occurs within 5−10 nm from the surface (Figure S10 in the Supporting Information).

(ii) Beyond $F_{1/2}$, the deep donor states can be assumed to be fully ionized and the charge density can be approximated as a constant equal to N_D, and an abrupt region is formed. The high density of charged deep donor states results in a very narrow space charge region analogous to a degenerately n-doped (n^+) semiconductor with $N = 10^{19}$−10^{20} cm^{-3}. The barrier height of the abrupt space charge region (Ψ_D) can be theoretically expressed as $\Psi_D = (E_D - \ln(1/g_D)k_BT) - E_g$. For a singly to triply degenerate state, and E_g = 0.83 eV, we obtain a theoretical value of $\Psi_D = 350 \pm 2$ meV. Experimentally, Ψ_D can be calculated from the EIS data independent of the state degeneracy, by subtraction of E_{FB}* from the apparent valence band edge potential to yield Ψ_D = 350 meV, which is in good agreement with our theoretical calculation. The abrupt space charge region width (W_D) can be calculated using the classical single-junction approximation: $W_D = (2\varepsilon_0\varepsilon_S\psi_{ac}/eN_{DS})^{1/2}$, since the charge density dependence only reaches a weak inversion. This equation yields a theoretical W_D of about 1.4 nm for a surface Fermi level pinned at the valence band edge. The experimental profile for the abrupt space charge region was generated from the EIS fitting results for C_{SC} vs V (Figure 9a, b) by calculating the apparent charge density in the abrupt space charge region [N_{SC} (V)] and the variable abrupt space charge depth (X_D) using eq 9 and the ideal capacitor equation: $X_D(V) = (\varepsilon_0\varepsilon_S)/C_{SC}(V)$. This profile, shown in Figure 10b was modeled as a double sided junction between the depletion and inversion region in the abrupt space charge region to account for the change in capacitance due to the contribution of valence band holes to the charge density within the inversion region. Note that at the edge of the abrupt space charge region X_D reaches a minimum given by the characteristic Debye length (L_D) for the bulk deep donor states (vertical black dash line in Figure 10b), which describes the falloff of the deep donor state band [$N_D(x)$ falloff], while N_{SC} reaches a maximum given by eq 10.[92] Figure 10b displays three distinctive regimes that can be identified as the edge of the abrupt space charge region, depletion region, and weak inversion region. In succession, these regimes illustrate how the charge density and the width of the abrupt space charge region changes as the surface Fermi level moves toward the valence band edge (vertical purple dash line in Figure 10b). In accordance with our previous discussion, the abrupt space charge region is preceded by the ionization of the deep donor states, followed by a resulting depletion region width of about 1 nm. Then, using our estimated valence band edge potential (E_V*), under surface Fermi level pinning we found a 3 Å weak inversion region and a total abrupt space charge width of W_D = 1.3 nm (the horizontal purple arrow in Figure 10b).

Energy Band Diagram and the Origin of Low Photovoltage. Figure 10c shows the energy band diagram for iron pyrite single crystals constructed by summarizing all of the results for the space charge properties. Note that, different from the hypothesized scheme in Figure 8a, all of the values shown in this diagram have been experimentally supported by one or multiple measurements. In addition, direct experimental evidence for a sharp surface band bending was obtained through AR-XPS analysis of S 2p peak. Our analysis of the space charge region clearly shows that the high-density bulk deep donor states have a more significant impact on the interfacial properties of iron pyrite than previously understood. The ionization of bulk deep states results in the formation of a very narrow (W_D = 1.3 nm) abrupt surface space charge region, which introduces a surface tunneling region and imposes a limitation to the barrier height of $\Psi_N \approx 230$ mV (Figure 10c). Furthermore, given the observed ultrafast carrier lifetime of τ = 300 ps, the high density of singly occupied deep donor states can be limiting the diffusion of minority carriers and introducing further limitations to the resulting space charge region with nonconstant charge distribution. Consequently, the ionization of bulk deep donor states results in a narrow abrupt surface space charge region that causes a limited V_{OC} and a lack of rectifying behavior, even if the surface states were passivated. Hence, despite a low *free* carrier concentration (10^{15} cm^{-3}) in the bulk, the high density (10^{20} cm^{-3}) and energetic distribution of the deep donor states impose limitations on iron pyrite single crystal solar cells that are in some sense similar to those usually ascribed to heavily doped semiconductors. In view of all the experimental evidence presented in this work, we found that the presence of a high density of deep donor states is the most satisfactory explanation for the poor photoconversion efficiency of iron pyrite single crystals. As the properties of the single crystals herein are comparable to those previously reported for synthetic iron pyrite crystals,[1,28,37,97] we can then generalize that the existence of intrinsic bulk defect states is the main factor limiting the performance of solar cells based on pyrite single crystals.

These findings have significant implications for the future development and application of iron pyrite single crystals, and also polycrystalline or nanocrystalline thin films as solar materials. These could also provide some ideas for understanding and improving other nonconventional semiconductor materials with low solar performance.[25−27] Upon comparison of the iron pyrite literature[36,37,49,64,98] with our evidence, it seems that intrinsic sulfur vacancies are the most reasonable and unifying explanation for the origin of the bulk deep states in iron pyrite. Under this assumption, the successful implementation of high temperature (above 450 °C) grown iron pyrite single crystals or thin films in solar cell technologies will depend on effective strategies to compensate for or avoid the formation of these sulfur vacancies. It has been previously suggested that the existence of sulfur vacancies in pyrite is due to a low energy of formation related to the thermal instability of iron pyrite.[36,53] Thus, an intuitive solution might be annealing iron pyrite crystals at a low temperature under a sulfur atmosphere. However, this proposal may not be practical because of the extremely sluggish self-diffusion of sulfur in iron pyrite at $T \leq 450$ °C.[99] An alternative strategy is to enhance pyrite's thermal stability and increase the energy of formation for bulk vacancies, potentially through the alloying of iron pyrite with other elements such as zinc and oxygen, or through the synthesis of related ternary compounds.[100−103] Still, the successful alloying of iron pyrite depends on the diffusivity and molar incorporation of the element of choice.

A more attractive strategy could be using iron pyrite materials grown at low temperature to reduce the density of bulk sulfur vacancies (thus defect states).[49] Low temperature synthesis may not be conducive to growing bulk single crystals or films with large crystalline domains. Therefore, nanocrystal-

line and polycrystalline pyrite films need to be utilized to fabricate efficient solar devices. On the basis of this study, *even if we can indeed avoid the formation of bulk sulfur vacancies*, the main limiting factor in the solar performance of such nanocrystalline and polycrystalline pyrite thin films then becomes the presence of surface defect states at the grain boundaries between crystalline domains with high surface area. The formation of a doubly pinned junction at the grain boundaries could lead to the accumulation of hole charge carriers at these boundaries, which will strongly dominate the conduction of these iron pyrite films and be quite detrimental due to nonuniform current distribution, high shunting resistance and fast carrier recombination. This can explain the apparent heavily p-like conductivity[43] and a lack of photovoltage[15,16,44] consistently reported for nanocrystalline and polycrystalline pyrite thin films. The effective passivation of polycrystalline pyrite thin films could also be achieved through the alloying of iron pyrite, or through the incorporation of compensating or passivating dopants that may preferentially segregated at grain boundaries. On the other hand, grain boundaries could be minimized through more elaborate nanostructuring approaches such as the fabrication of a vertical-aligned array of iron pyrite single crystal nanowires/microwires.[12,42] The single crystal iron pyrite nanostructures[42] could also offer a convenient platform[104] to investigate whether low synthetic temperatures will indeed provide a better opportunity to enable iron pyrite with less sulfur vacancies as a solar semiconductor. Such low temperature grown iron pyrite single crystals can allow the exploration of the Schottky buried junction (caused by intrinsic surface Fermi level pinning) as an intentional design for solar devices in the absence of bulk deep states, as our results have suggested.

CONCLUSIONS

We have integrated results from a variety of experimental techniques to show that the space charge properties of {100}-faceted *n*-type iron pyrite single crystals grown by CVT are dominated by the existence of a high density of deep donor states on the order of $N_D \approx 10^{20}$ cm^{-3} (despite a *free* carrier density of $N \approx 10^{15}$ cm^{-3}) and the surface acceptor states on the order of $N_{SS} \approx 10^{15}$ cm^{-2}. Our results suggest that the origin of the bulk deep states are related to intrinsic sulfur vacancies in iron pyrite and the surface states result from the intrinsic reduced coordination of the {100} surface of iron pyrite. The surface acceptor states dominate the interfacial charge equilibration of iron pyrite single crystals, strongly pinning the surface Fermi level near the valence band edge, and therefore, "buffering" changes in band bending and barrier height within a 2 V window in acetonitrile electrolytes. However, considering the charge neutrality condition and the observed energetic distribution of surface states with a maximum below the valence band edge, surface states are not responsible for the low photovoltage and low photoconversion efficiencies of iron pyrite single crystals, as it has been previously suggested.[1,23,38] In fact, the buried junction caused by the surface Fermi level pinning could perhaps be intentionally utilized for solar devices in the absence of bulk defect states. On the other hand, we found that the ionization of the bulk deep donor states in iron pyrite profoundly impacts the space charge, resulting in a region with a nonconstant distribution of ionized deep donor states and an abrupt region with a constant charge distribution equal to N_D. This results in a small barrier height of Ψ_N = 230 mV limited by an abrupt surface space charge region with a very narrow width of W_D = 1.3 nm. Despite a space charge width of W_N = 40 nm, about 130 mV of this Ψ_N actually occurs within 10 nm from the surface. Furthermore, the observed ultrafast carrier lifetime suggests that the high density of deep donor states can limit the diffusion of minority carriers within the nonconstant space charge region. By synthesizing all of these results, our work shows that the low photovoltage and low solar conversion efficiency of iron pyrite single crystals can be mainly attributed to the presence of intrinsic bulk deep donor states in high density, likely caused by bulk sulfur vacancies. Consequently, in order to enable single crystal iron pyrite as a solar material, the intrinsic bulk states must be treated first, either by avoiding their formation or through bulk compensation strategies. Furthermore, in the case of polycrystalline and nanocrystalline pyrite films, overcoming bulk defect states might not be sufficient due to the potential detrimental effects of surface defect states at the grain boundaries.

ASSOCIATED CONTENT

Supporting Information

Experimental details, additional figures and discussion. This material is available free of charge via the Internet at http://pubs.acs.org.

AUTHOR INFORMATION

Corresponding Author

jin@chem.wisc.edu

Notes

The authors declare no competing financial interest.

ACKNOWLEDGMENTS

The research was supported by the U.S. Department of Energy, SunShot NextGen PV II program under Award DE-EE0005330 (to S.J.). M.C.-A. thanks the NSF Graduate Research Fellowship for support. S.J., R.J.H., J.C.W., C.R.E., B.J.T., and K.J.C. also thank the U.S. Department of Energy, Office of Basic Energy Sciences, Division of Materials Sciences and Engineering, under Award DE-FG02-09ER46664 for support of the diverse spectroscopic and surface analysis of the materials. S.J. also thanks the Research Corporation Scialog Award for Solar Energy Conversion and UW−Madison Vilas Associate Award for support. XPS characterization was performed on instrumentation supported by the UW−Madison College of Engineering, Materials Research Science and Engineering Center (NSF DMR-1121288), and Nanoscale Science and Engineering Center (NSF DMR-0832760). We thank Ms. Melinda Shearer for assistance with XPS measurements. We thank Ms. Kristin Stafford and Prof. Kyoung-Shin Choi for their assistance with the UV−vis−NIR measurements.

REFERENCES

(1) Ennaoui, A.; Fiechter, S.; Pettenkofer, C.; Alonso-Vante, N.; Büker, K.; Bronold, M.; Höpfner, C.; Tributsch, H. *Sol. Energy Mater. Sol. Cells* **1993**, *29*, 289.

(2) Ennaoui, A.; Fiechter, S.; Goslowsky, H.; Tributsch, H. *J. Electrochem. Soc.* **1985**, *132*, 1579.

(3) Altermatt, P. P.; Kiesewetter, T.; Ellmer, K.; Tributsch, H. *Sol. Energy Mater. Sol. Cells* **2002**, *71*, 181.

(4) Ennaoui, A.; Tributsch, H. *Sol. Energy Mater.* **1986**, *14*, 461.

(5) Buker, K.; Alonso-Vante, N.; Scheer, R.; Tributsch, H. *Ber. Bunsen-Ges.* **1994**, *98*, 674.

(6) Wadia, C.; Alivisatos, A. P.; Kammen, D. M. *Environ. Sci. Technol.* **2009**, *43*, 2072.
(7) Lehner, S.; Savage, K.; Ciobanu, M.; Cliffel, D. E. *Geochim. Cosmochim. Acta* **2007**, *71*, 2491.
(8) Fiechter, S.; Mai, J.; Ennaoui, A.; Szacki, W. *J. Cryst. Growth* **1986**, *78*, 438.
(9) Seefeld, S.; Limpinsel, M.; Liu, Y.; Farhi, N.; Weber, A.; Zhang, Y.; Berry, N.; Kwon, Y. J.; Perkins, C. L.; Hemminger, J. C.; Wu, R.; Law, M. *J. Am. Chem. Soc.* **2013**, *135*, 4412.
(10) Höpfner, C.; Ellmer, K.; Ennaoui, A.; Pettenkofer, C.; Fiechter, S.; Tributsch, H. *J. Cryst. Growth* **1995**, *151*, 325.
(11) Berry, N.; Cheng, M.; Perkins, C. L.; Limpinsel, M.; Hemminger, J. C.; Law, M. *Adv. Energy Mater.* **2012**, *2*, 1124.
(12) Cabán-Acevedo, M.; Faber, M. S.; Tan, Y.; Hamers, R. J.; Jin, S. *Nano Lett.* **2012**, *12*, 1977.
(13) Pimenta, G.; Kautek, W. *Thin Solid Films* **1992**, *219*, 37.
(14) Li, L.; Caban-Acevedo, M.; Girard, S. N.; Jin, S. *Nanoscale* **2014**, *6*, 2112.
(15) Morrish, R.; Silverstein, R.; Wolden, C. A. *J. Am. Chem. Soc.* **2012**, *134*, 17854.
(16) Bi, Y.; Yuan, Y.; Exstrom, C. L.; Darveau, S. A.; Huang, J. *Nano Lett.* **2011**, *11*, 4953.
(17) Wadia, C.; Wu, Y.; Gul, S.; Volkman, S. K.; Guo, J.; Alivisatos, A. P. *Chem. Mater.* **2009**, *21*, 2568.
(18) Puthussery, J.; Seefeld, S.; Berry, N.; Gibbs, M.; Law, M. *J. Am. Chem. Soc.* **2010**, *133*, 716.
(19) Macpherson, H. A.; Stoldt, C. R. *ACS Nano* **2012**, *6*, 8940.
(20) Lucas, J. M.; Tuan, C.-C.; Lounis, S. D.; Britt, D. K.; Qiao, R.; Yang, W.; Lanzara, A.; Alivisatos, A. P. *Chem. Mater.* **2013**, *25*, 1615.
(21) Wang, D.-Y.; Jiang, Y.-T.; Lin, C.-C.; Li, S.-S.; Wang, Y.-T.; Chen, C.-C.; Chen, C.-W. *Adv. Mater. (Weinheim, Ger.)* **2012**, *24*, 3415.
(22) Kirkeminde, A.; Ren, S. *J. Mater. Chem. A* **2013**, *1*, 49.
(23) Ennaoui, A.; Fiechter, S.; Smestad, G.; Tributsch, H. In *Energy and the Environment: Into the 1990s*; Sayigh, A. A. M., Ed.; Pergamon Press: London, 1990.
(24) Buker, K.; Alonso-Vante, N.; Tributsch, H. *J. Appl. Phys.* **1992**, *72*, 5721.
(25) Walter, M. G.; Warren, E. L.; McKone, J. R.; Boettcher, S. W.; Mi, Q.; Santori, E. A.; Lewis, N. S. *Chem. Rev.* **2010**, *110*, 6446.
(26) Unold, T.; Schock, H. W. *Annu. Rev. Mater. Res.* **2011**, *41*, 297.
(27) Mayer, M. T.; Lin, Y.; Yuan, G.; Wang, D. *Acc. Chem. Res.* **2013**, *46*, 1558.
(28) Ennaoui, A.; Fiechter, S.; Jaegermann, W.; Tributsch, H. *J. Electrochem. Soc.* **1986**, *133*, 97.
(29) Pettenkofer, C.; Jaegermann, W.; Bronold, M. *Ber. Bunsen-Ges.* **1991**, *95*, 560.
(30) Nesbitt, H. W.; Uhlig, I.; Bancroft, G. M.; Szargan, R. *Am. Mineral.* **2004**, *88*, 1279.
(31) Herbert, F. W.; Krishnamoorthy, A.; Van Vliet, K. J.; Yildiz, B. *Surf. Sci.* **2013**, *618*, 53.
(32) Alonso-Vante, N.; Chatzitheodorou, G.; Fiechter, S.; Mgoduka, N.; Poulios, I.; Tributsch, H. *Solar Energy Mater.* **1988**, *18*, 9.
(33) Bungs, M.; Tributsch, H. *Ber. Bunsen-Ges.* **1997**, *101*, 1844.
(34) Bronold, M.; Buker, K.; Kubala, S.; Pettenkofer, C.; Tributsch, H. *Phys. Status Solidi A* **1993**, *135*, 231.
(35) Bronold, M.; Tomm, Y.; Jaegermann, W. *Surf. Sci.* **1994**, *314*, L931.
(36) Birkholz, M.; Fiechter, S.; Hartmann, A.; Tributsch, H. *Phys. Rev. B* **1991**, *43*, 11926.
(37) Bronold, M.; Pettenkofer, C.; Jaegermann, W. *J. Appl. Phys.* **1994**, *76*, 5800.
(38) Limpinsel, M.; Farhi, N.; Berry, N.; Lindemuth, J.; Perkins, C. L.; Lin, Q.; Law, M. *Energy Environ. Sci.* **2014**, *7*, 1974.
(39) Lewis, N. S. *J. Electrochem. Soc.* **1984**, *131*, 2496.
(40) Nagasubramanian, G.; Bard, A. J. *J. Electrochem. Soc.* **1981**, *128*, 1055.
(41) Grimm, R. L.; Bierman, M. J.; O'Leary, L. E.; Strandwitz, N. C.; Brunschwig, B. S.; Lewis, N. S. *J. Phys. Chem. C* **2012**, *116*, 23569.
(42) Cabán-Acevedo, M.; Liang, D.; Chew, K. S.; DeGrave, J. P.; Kaiser, N. S.; Jin, S. *ACS Nano* **2013**, *7*, 1731.
(43) Ferrer, I. J.; Ares, J. R.; Sánchez, C. R. *Sol. Energy Mater. Sol. Cells* **2003**, *76*, 183.
(44) Steinhagen, C.; Harvey, T. B.; Stolle, C. J.; Harris, J.; Korgel, B. A. *J. Phys. Chem. Lett.* **2012**, *3*, 2352.
(45) Kleppe, A. K.; Jephcoat, A. P. *Mineral. Mag.* **2004**, *68*, 433.
(46) Vogt, H.; Chattopadhyay, T.; Stolz, H. J. *J. Phys. Chem. Solids* **1983**, *44*, 869.
(47) Lennie, A. R.; Vaughan, D. J. *Am. Mineral.* **1992**, *77*, 1166.
(48) Sze, S. M. *Physics of Semiconductor Devices*; John Wiley & Sons: New York, 1981.
(49) Fiechter, S.; Birkholz, M.; Hartmann, A.; Dulski, P.; Giersig, M.; Tributsch, H.; Tilley, R. J. D. *J. Mater. Res.* **1992**, *7*, 1829.
(50) Mott, N. F. *Mott-Insulator Transition*; 2nd ed.; Taylor-Francis: London, 1990.
(51) Koon, D. W.; Castner, T. G. *Solid State Commun.* **1987**, *64*, 4.
(52) Mott, N. F. *J. Phys. Colloques* **1976**, *37*, C4.
(53) Shklovskii, B. I.; Efros, A. L. *Electronic Properties of Doped Semiconductors*; Springer-Verlag: Berlin, 1984.
(54) Lichtenberger, D.; Ellmer, K.; Schieck, R.; Fiechter, S.; Tributsch, H. *Thin Solid Films* **1994**, *246*, 6.
(55) Zhang, X.; Manno, M.; Baruth, A.; Johnson, M.; Aydil, E. S.; Leighton, C. *ACS Nano* **2013**, *7*, 2781.
(56) Pollak, M.; Shklovskii, B. I. *Hopping Transport in Solids*; Elsevier Science: Amsterdam, 1991; Vol. *28*.
(57) Gruenewald, M.; Mueller, H.; Thomas, P.; Wuertz, D. *Solid State Commun.* **1981**, *38*, 4.
(58) Hung, C. S.; Gliessman, J. R. *Phys. Rev.* **1950**, *79*, 726.
(59) Fritzsche, H.; Lark-Horovitz, K. *Phys. Rev.* **1955**, *99*, 400.
(60) Simmons, J. H.; Potter, K. S. *Optical Materials*; Academic: San Diego, CA, 2000.
(61) Urbach, F. *Phys. Rev.* **1953**, *92*, 1324.
(62) Ferrer, I. J.; Nevskaia, D. M.; Delasheras, C.; Sánchez, C. *Solid State Commun.* **1990**, *74*, 913.
(63) Kronik, L.; Shapira, Y. *Surf. Sci. Rep.* **1999**, *37*, 1.
(64) Kolb, B.; Kolpak, A. M. *Phys. Rev. B* **2013**, *88*, 235208.
(65) Salvador, P.; Tafalla, D.; Tributsch, H.; Wetzel, H. *J. Electrochem. Soc.* **1991**, *138*, 3361.
(66) Buker, K.; Alonso-Vante, N.; Tributsch, H. *Ber. Bunsen-Ges.* **1996**, *100*, 1808.
(67) Wang, Y.-C.; Wang, D.-Y.; Jiang, Y.-T.; Chen, H.-A.; Chen, C.-C.; Ho, K.-C.; Chou, H.-L.; Chen, C.-W. *Angew. Chem., Int. Ed.* **2013**, *52*, 6694.
(68) Faber, M. S.; Dziedzic, R.; Lukowski, M. A.; Kaiser, N. S.; Ding, Q.; Jin, S. *J. Am. Chem. Soc.* **2014**, *136*, 10053.
(69) Lowson, R. T. *Chem. Rev.* **1982**, *82*, 461.
(70) Moses, C. O.; Kirk Nordstrom, D.; Herman, J. S.; Mills, A. L. *Geochim. Cosmochim. Acta* **1987**, *51*, 1561.
(71) Bard, A. J.; Bocarsly, A. B.; Fan, F. R. F.; Walton, E. G.; Wrighton, M. S. *J. Am. Chem. Soc.* **1980**, *102*, 3671.
(72) Sinn, C.; Meissner, D.; Memming, R. *J. Electrochem. Soc.* **1990**, *137*, 168.
(73) Memming, R. *Semiconductor Electrochemistry*; Wiley-VCH: Weinheim, 2001.
(74) Kühne, H.-M.; Tributsch, H. *J. Electroanal. Chem. Interfacial Electrochem.* **1986**, *201*, 263.
(75) Yeh, J. J.; Lindau, I. *At. Data. Nucl. Data Tables* **1985**, *32*, 1.
(76) Nesbitt, H. W.; Bancroft, G. M.; Pratt, A. R.; Scaini, M. J. *Am. Mineral.* **1998**, *83*, 1067.
(77) Andersson, K.; Nyberg, M.; Ogasawara, H.; Nordlund, D.; Kendelewicz, T.; Doyle, C. S.; Brown, G. E.; Pettersson, L. G. M.; Nilsson, A. *Phys. Rev. B* **2004**, *70*, 195404.
(78) Aizawa, T.; Suehara, S.; Hishita, S.; Otani, S.; Arai, M. *Phys. Rev. B* **2005**, *71*, 165405.
(79) Herbert, F. W.; Krishnamoorthy, A.; Ma, W.; Van Vliet, K. J.; Yildiz, B. *Electrochim. Acta* **2014**, *127*, 416.

(80) Powell, C. J.; Jablonski, A. *NIST Electron Inelastic-Mean-Free-Path Database*, Version 1.2, SRD 71; National Institute of Standards and Technology: Gaithersburg, MD, 2010.
(81) Cooper, J. W. *Phys. Rev. A* **1993**, *47*, 1841.
(82) Pavlychev, A. A.; Fominykh, N. G. *J. Phys.: Condens. Matter* **1996**, *8*, 2305.
(83) Chen, Y. F. *Surf. Sci. Rep.* **2002**, *519*, 115.
(84) von Oertzen, G. U.; Skinner, W. M.; Nesbitt, H. W. *Radiat. Phys. Chem.* **2006**, *75*, 1855.
(85) Sharma, J.; Staley, R. H.; Rimstidt, J. D.; Fair, H. D.; Gora, T. F. *Chem. Phys. Lett.* **1971**, *9*, 564.
(86) Schlaf, R.; Hinogami, R.; Fujitani, M.; Yae, S.; Nakato, Y. *J. Vac. Sci. Technol., A* **1999**, *17*, 164.
(87) Klahr, B.; Gimenez, S.; Fabregat-Santiago, F.; Hamann, T.; Bisquert, J. *J. Am. Chem. Soc.* **2012**, *134*, 4294.
(88) Mora-Seró, I.; Garcia-Belmonte, G.; Boix, P. P.; Vazquez, M. A.; Bisquert, J. *Energy Environ. Sci.* **2009**, *2*, 678.
(89) Mora-Seró, I.; Luo, Y.; Garcia-Belmonte, G.; Bisquert, J.; Muñoz, D.; Voz, C.; Puigdollers, J.; Alcubilla, R. *Sol. Energy Mater. Sol. Cells* **2008**, *92*, 505.
(90) Bisquert, J. *Phys. Chem. Chem. Phys.* **2003**, *5*, 5360.
(91) Heath, J. T.; Cohen, J. D.; Shafarman, W. N. *J. Appl. Phys.* **2004**, *95*, 1000.
(92) Blood, P. *Semicond. Sci. Technol.* **1986**, *1*, 7.
(93) Kimerling, L. C. *J. Appl. Phys.* **1974**, *45*, 1839.
(94) Kelly, J. J.; Memming, R. *J. Electrochem. Soc.* **1982**, *129*, 730.
(95) Schröder, K.; Memming, R. *Ber. Bunsen-Ges.* **1985**, *89*, 385.
(96) Bard, A. J.; Faulkner, L. R. *Electrochemical Methods: Fundamentals and Application*; Wiley & Sons: New York, 2001.
(97) Buker, K.; Alonso-Vante, N.; Tributsch, H. *J. Appl. Phys.* **1992**, *72*, 5721.
(98) de las Heras, C.; de Vidales, J. L. M.; Ferrer, I. J.; Sánchez, C. *J. Mater. Res.* **1996**, *11*, 211.
(99) Watson, E. B.; Cherniak, D. J.; Frank, E. A. *Geochim. Cosmochim. Acta* **2009**, *73*, 4792.
(100) Mao, B.; Dong, Q.; Xiao, Z.; Exstrom, C. L.; Darveau, S. A.; Webber, T. E.; Lund, B. D.; Huang, H.; Kang, Z.; Huang, J. *J. Mater. Chem. A* **2013**, *1*, 12060.
(101) Yu, L.; Lany, S.; Kykyneshi, R.; Jieratum, V.; Ravichandran, R.; Pelatt, B.; Altschul, E.; Platt, H. A. S.; Wager, J. F.; Keszler, D. A.; Zunger, A. *Adv. Energy Mater.* **2011**, *1*, 748.
(102) Hu, J.; Zhang, Y.; Law, M.; Wu, R. *J. Am. Chem. Soc.* **2012**, *134*, 13216.
(103) Sun, R.; Ceder, G. *Phys. Rev. B* **2011**, *84*, 245211.
(104) Liang, D.; Cabán-Acevedo, M.; Kaiser, N. S.; Jin, S. *Nano Lett.* **2014**, *14*, DOI: 10.1021/nl501942w.